Thermal Hall responses in frustrated honeycomb spin systems

Kosuke Fujiwara [1], Sota Kitamura [1], and Takahiro Morimoto [1,2]
[1] *Department of Applied Physics, The University of Tokyo, Hongo, Tokyo 113-8656, Japan*
[2] *JST, PRESTO, Kawaguchi, Saitama 332-0012, Japan*

(Received 8 April 2022; revised 22 June 2022; accepted 27 June 2022; published 11 July 2022)

We study geometrical responses of magnons driven by a temperature gradient in frustrated spin systems. While Dzyaloshinskii-Moriya (DM) interactions are usually incorporated to obtain geometrically nontrivial magnon bands, here we investigate thermal Hall responses of magnons that do not rely on the DM interactions. Specifically, we focus on frustrated spin systems with sublattice degrees of freedom and show that a nonzero Berry curvature requires breaking of an effective PT symmetry. According to this symmetry consideration, we study the J_1-J_2-J_2' Heisenberg models on a honeycomb lattice as a representative example and demonstrate that magnons in the spiral phase support the thermal Hall effect once we introduce a magnetic field and asymmetry between the two sublattices. We also show that driving the magnons by a temperature gradient induces spin current generation (i.e., magnon spin Nernst effect) in the J_1-J_2-J_2' Heisenberg models.

DOI: 10.1103/PhysRevB.106.035113

I. INTRODUCTION

A magnon is an elementary excitation of spin waves in magnetic materials. Magnon transport is attracting growing interest in both fundamental and technological aspects [1]. For example, magnons can transfer spins without Joule heating and are expected to play an essential role in spintronics as a platform for low energy consumption devices. In particular, antiferromagnetic spintronics is attracting a keen attention because antiferromagnets have no leakage magnetic field in contrast to conventional ferromagnets [2,3].

Since magnons are charge neutral quasiparticles, they cannot be directly driven by electric fields, unlike electrons. Instead, a temperature gradient can induce a magnon flow, which leads to various thermal responses in magnets, including the spin Seebeck effect [4], the magnon spin Nernst effect [5–7], and the thermal Hall effect [8,9]. The thermal Hall effect and the magnon spin Nernst effect are of particular interest because they are related to a nontrivial geometry of the magnon bands through the Berry curvature [5,6,10–13].

Most previous studies on such geometrical thermal responses of magnons rely on Dzyaloshinskii-Moriya (DM) interactions to obtain geometrically nontrivial magnon bands with nonzero Berry curvature. For example, the thermal Hall effect has been studied in an antiferromagnetic Heisenberg model with DM interactions on a kagome lattice [14–18] and a honeycomb lattice [19]. Similarly, the magnon spin Nernst effect has been studied in a Heisenberg model with a DM interaction [5,6,13].

The DM interaction introduces a nontrivial geometry to magnon bands in two fashions. First, the DM interaction acts as a virtual magnetic field for magnons, leading to nonzero Berry curvature [8,20]. In this case, there exists a condition for the lattice geometry to support nonzero Berry curvature because edge-shared lattices results in cancellation of such virtual magnetic field between the neighboring plaquettes. For example, a kagome lattice supports a thermal Hall response with this mechanism. Second, the DM interaction can also introduce an effective non-Abelian gauge field for magnons with multiple internal degrees of freedom. In particular, when we consider a bipartite lattice with AB sublattices, the DM interaction can behave as an SU(2) gauge field for the sublattice degree of freedom. This mechanism is advantageous over the first one in that the lattice geometry is not restricted [21]. In both cases, however, the DM interaction is usually small except for a few limited systems because the DM interaction originates from the spin-orbit interaction [22,23]. Therefore, geometrically nontrivial magnon bands that do not rely on the presence of the DM interaction are desired for an enhancement of thermal Hall responses in magnetic systems.

Such geometrical responses of magnons without DM interactions were reported in a few studies. Scalar spin chirality is shown to support the thermal Hall effect for the honeycomb lattice by assuming a particular ground state spin configuration [24], for the kagome lattice by incorporating a third neighbor coupling [25,26], and for the trimerized triangular lattice [27]. The scalar spin chirality has been also shown to support the spinon thermal Hall conductivity of chiral spin liquid in the honeycomb lattice [28]. Another previous study reports that some organic materials [29–31] support geometrical magnon responses driven by temperature gradient due to special properties of dimers. Despite these previous studies, a guiding principle for realizing geometrical thermal responses of magnons without the DM interaction is still missing. In particular, the possibility of nontrivial magnon bands originating from an SU(2) gauge field without DM interaction has not been fully explored.

In this paper, we study geometrical thermal responses of magnons that do not rely on the DM interaction. Specifically, we focus on the antiferromagnetic Heisenberg model with AB

sublattices. As the sublattice degrees of freedom enables to introduce the SU(2) gauge field to the magnons, this model is a suitable playground for pursuing the role of the non-Abelian gauge field on the geometrically nontrivial magnon bands. We first derive a general condition for generating nonzero Berry curvature without the DM interaction. We find that an effective PT symmetry should be broken for obtaining geometrically nontrivial bands, and a noncollinear spin structure is necessary to break this PT-symmetry. From this viewpoint, frustrated spin systems are suitable for pursuing noncollinear spin configurations [32–34]. Thus we consider geometrical thermal responses in a frustrated honeycomb spin systems as a simple example. Specifically, we study the J_1-J_2-J_2' Heisenberg model on the honeycomb lattice. The frustration naturally leads to the spiral order in the ground state and support the nonzero Berry curvature. Furthermore, we also consider spin transport enabled by nontrivial magnon bands, i.e., the magnon spin Nernst effect. In the noncollinear system, the magnon spin Nernst effect is governed by a quantity that is closely related to the Berry curvature [35,36]. We demonstrate that the frustrated honeycomb Heisenberg model also supports the magnon spin Nernst effect without DM interaction.

The rest of this paper is organized as follows. In Sec. II, we study magnon excitations using the Holstein-Primakoff transformation for the spiral phase with AB sublattices and derive the symmetry condition that the Berry curvature and the thermal Hall conductivity appear. In Sec. III, we consider the J_1-J_2-J_2' model on the honeycomb lattice and study the thermal Hall conductivity. In Sec. IV, we study the spin Nernst effect of J_1-J_2-J_2' model. In Sec. V, we present a brief discussion.

II. MAGNON HAMILTONIAN IN SPIRAL PHASE

In this section, we consider the condition for the nonzero Berry curvature and the thermal Hall conductivity in the AB sublattice systems. First, to calculate the thermal Hall effect, we review the magnon expansion in AB sublattice systems. Then we introduce the formulation of the thermal Hall effect of magnons. After these preparations, we derive a general condition for generating nonzero thermal Hall effect.

A. Magnon Hamiltonian of *AB* sublattices

We study the magnon Hamiltonian of the system with AB sublattices. To obtain the magnon Hamiltonian, we perform the Holstein-Primakoff transformation for the spin S systems [37],

$$\begin{aligned} S_i'^{+} &\simeq \sqrt{2S}a_i, S_i'^{-} \simeq \sqrt{2S}a_i^\dagger, S_i'^{z} = S - a_i^\dagger a_i \quad \text{for } i \in A \\ S_i'^{+} &\simeq \sqrt{2S}b_i, S_i'^{-} \simeq \sqrt{2S}b_i^\dagger, S_i'^{z} = S - b_i^\dagger b_i \quad \text{for } i \in B, \end{aligned} \tag{1}$$

where $a_i^\dagger$ and $b_i^\dagger$ are bosonic creation operators, $\boldsymbol{S}'$ is a spin operator along the spin configuration of the ground state, and $S_i'^{\pm} = S_i'^x \pm iS_i'^y$. For a system in which the ground state is not ferromagnetic, the magnon Hamiltonian contains $\alpha_i^\dagger\alpha_j^\dagger$ and $\alpha_i\alpha_j$ terms with α_i being a_i or b_i. Thus, after the Fourier transformation, we obtain the magnon Hamiltonian as a 4×4 matrix:

$$H = \frac{1}{2}\sum_{\boldsymbol{k}} \Psi^\dagger(\boldsymbol{k})H(\boldsymbol{k})\Psi(\boldsymbol{k}). \tag{2}$$

This type of Hamiltonian is called the Bogoliubov–de Gennes (BdG) Hamiltonian [38]. Here, $\Psi(\boldsymbol{k})$ and $H(\boldsymbol{k})$ are

$$\Psi(\boldsymbol{k}) = (a(\boldsymbol{k}), b(\boldsymbol{k}), a^\dagger(-\boldsymbol{k}), b^\dagger(-\boldsymbol{k}))^T, \tag{3}$$

$$H(\boldsymbol{k}) = \begin{pmatrix} \Xi(\boldsymbol{k}) & \Pi(\boldsymbol{k}) \\ \Pi^*(-\boldsymbol{k}) & \Xi^*(-\boldsymbol{k}) \end{pmatrix}, \tag{4}$$

where $\Xi(\boldsymbol{k})$ and $\Pi(\boldsymbol{k})$ are 2×2 matrices that satisfy $\Xi^\dagger(\boldsymbol{k}) = \Xi(\boldsymbol{k})$, $\Pi^\dagger(\boldsymbol{k}) = \Pi^*(-\boldsymbol{k})$. Using Pauli matrices, we can write $\Xi(\boldsymbol{k})$ and $\Pi(\boldsymbol{k})$ as

$$\Xi(\boldsymbol{k}) = \Xi^0(\boldsymbol{k})\sigma_0 + \Xi^x(\boldsymbol{k})\sigma_x + \Xi^y(\boldsymbol{k})\sigma_y + \Xi^z(\boldsymbol{k})\sigma_z, \tag{5}$$

$$\Pi(\boldsymbol{k}) = \Pi^0(\boldsymbol{k})\sigma_0 + \Pi^x(\boldsymbol{k})\sigma_x + \Pi^y(\boldsymbol{k})\sigma_y + \Pi^z(\boldsymbol{k})\sigma_z, \tag{6}$$

with $\Xi^i \in \mathbb{R}$ and $\Pi^i \in \mathbb{C}$ $(i = 0, x, y, z)$. The BdG Hamiltonian should be diagonalized using a paraunitary matrix $T(\boldsymbol{k})$, which satisfies

$$\begin{aligned} &T^\dagger(\boldsymbol{k})\sigma_3 T(\boldsymbol{k}) = \sigma_3, \\ &\sigma_3 = \begin{pmatrix} 1 & 0 & 0 & 0 \\ 0 & 1 & 0 & 0 \\ 0 & 0 & -1 & 0 \\ 0 & 0 & 0 & -1 \end{pmatrix}, \end{aligned} \tag{7}$$

so as to retain the canonical commutation relation for the transformed magnon operator $T^{-1}(\boldsymbol{k})\Psi(\boldsymbol{k})$. The eigenvalues have the following form due to the inherent particle-hole symmetry as:

$$\begin{aligned} T^\dagger(\boldsymbol{k})H(\boldsymbol{k})T(\boldsymbol{k}) &= E(\boldsymbol{k}) \\ &= \text{diag}(E_1(\boldsymbol{k}), E_2(\boldsymbol{k}), E_1(-\boldsymbol{k}), E_2(-\boldsymbol{k})). \end{aligned} \tag{8}$$

Applying $T(\boldsymbol{k})\sigma_3$ to Eq. (8), we obtain

$$\sigma_3 H(\boldsymbol{k})T(\boldsymbol{k}) = T(\boldsymbol{k})\sigma_3 E(\boldsymbol{k}), \tag{9}$$

namely, we can obtain $T(\boldsymbol{k})$ as eigenvectors of $\sigma_3 H$. If we write the paraunitary matrix $T(\boldsymbol{k})$ as

$$T(\boldsymbol{k}) = (\boldsymbol{t}_1(\boldsymbol{k}), \boldsymbol{t}_2(\boldsymbol{k}), \boldsymbol{t}_3(\boldsymbol{k}), \boldsymbol{t}_4(\boldsymbol{k})), \tag{10}$$

we can write Eq. (9) in the form of an eigenvalue problem for $\sigma_3 H$ as

$$\sigma_3 H(\boldsymbol{k})\boldsymbol{t}_n(\boldsymbol{k}) = (\sigma_3 E(\boldsymbol{k}))_{nn}\boldsymbol{t}_n(\boldsymbol{k}). \tag{11}$$

B. Thermal Hall effect and Berry curvature

We calculate the thermal Hall conductivity by using the linear response theory. The temperature gradient is written as $T(\boldsymbol{r}) = T_0(1 - \chi(\boldsymbol{r}))$, where T_0 is a constant temperature and χ is a small parameter with a zero average. We write the thermal Hall current J_μ^Q as

$$J_\mu^Q = L_{\mu\nu}\left(T\nabla_\nu \frac{1}{T} - \nabla_\nu \chi\right),$$

and the thermal Hall conductivity $\kappa_{\mu\nu}$ as

$$\kappa_{\mu\nu} = \frac{L_{\mu\nu}}{T}.$$

From a continuity equation, we can calculate the thermal current, and using the Kubo formula, we can write the thermal Hall conductivity $\kappa_{\mu\nu}$ as [12]

$$\kappa_{\mu\nu} = -\frac{k_B^2 T}{\hbar}\sum_{n=1,2}\int_{BZ}\frac{dk^2}{(2\pi)^2}\Omega(\boldsymbol{k})_{n,\mu\nu} \times \left[c_2(\rho(E_n(\boldsymbol{k}))) - \frac{\pi^2}{3}\right], \tag{12}$$

with

$$c_2(x) = \int_0^x dt\left(\ln\frac{1+t}{t}\right)^2 = (1+x)\left(\ln\frac{1+x}{x}\right)^2 - (\ln x)^2 - 2\mathrm{Li}_2(-x),$$

and $\mathrm{Li}_n(x)$ is polylogarithm function. $\Omega(\boldsymbol{k})_{n,\mu\nu}$ is the Berry curvature of the nth magnon band,

$$\Omega_{n,\mu\nu}(\boldsymbol{k}) = -2\mathrm{Im}\left[\sigma_3\frac{\partial T^\dagger(\boldsymbol{k})}{\partial k_\mu}\sigma_3\frac{\partial T(\boldsymbol{k})}{\partial k_\nu}\right]_{nn}, \tag{13}$$

which measures a nontrivial band geometry.

C. Effective *PT* and *T* symmetries

Symmetry plays an important role in the emergence of nontrivial magnon bands with Berry curvature. In particular, we find that the Berry curvature of magnon bands vanishes under an effective PT symmetry in a similar manner to the Berry curvature in electronic systems. In this subsection, we derive a symmetry condition for the nonzero Berry curvature and thermal Hall conductivity.

Let us suppose that the system has a symmetry given by

$$P^\dagger H^*(\boldsymbol{k})P = H(\boldsymbol{k}), \tag{14}$$

with a paraunitary matrix P satisfying $P^\dagger\sigma_3 P = \sigma_3$. By utilizing Eq. (14), we can rewrite Eq. (9) as

$$\sigma_3 H(k)P^*T^*(\boldsymbol{k}) = P^*T^*(\boldsymbol{k})\sigma_3 E(\boldsymbol{k}), \tag{15}$$

which implies that $P^*T^*(\boldsymbol{k})$ satisfies the same Eq. (9) for $T(\boldsymbol{k})$. Thus, if there is no degeneracy, $T(\boldsymbol{k})$ should satisfy

$$T(\boldsymbol{k}) = P^*T^*(\boldsymbol{k})M_{\boldsymbol{k}}, \tag{16}$$

where $(M_{\boldsymbol{k}})_{j,l} = \delta_{j,l}\exp[i\theta_{j,\boldsymbol{k}}]$ comes from the fact that we can choose the overall phases of the eigenvectors arbitrarily.

We investigate how this symmetry operation affects the Berry curvature. Considering the condition Eq. (16), the Berry curvature Eq. (13) can be written as

$$\begin{aligned}\Omega_{n,\mu\nu}(\boldsymbol{k}) &= -2\mathrm{Im}\left[\sigma_3\frac{\partial T^\dagger(\boldsymbol{k})}{\partial k_\mu}\sigma_3\frac{\partial T(\boldsymbol{k})}{\partial k_\nu}\right]_{nn}\\ &= -2\mathrm{Im}\left[\sigma_3\frac{\partial M_{\boldsymbol{k}}^\dagger T^{\dagger *}(\boldsymbol{k})}{\partial k_\mu}P^{*\dagger}\sigma_3 P^*\frac{\partial T^*(\boldsymbol{k})M_{\boldsymbol{k}}}{\partial k_\nu}\right]_{nn}\\ &= 2\mathrm{Im}\left[\sigma_3\frac{\partial T^\dagger(\boldsymbol{k})}{\partial k_\mu}\sigma_3\frac{\partial T(\boldsymbol{k})}{\partial k_\nu}\right]_{nn}\\ &= -\Omega_{n,\mu\nu}(\boldsymbol{k}).\end{aligned} \tag{17}$$

Therefore, the Berry curvature becomes zero under the symmetry Eq. (14).

Even if the Berry curvature takes nonzero value, the thermal Hall conductivity can vanish in some cases when the integral in Eq. (12) has a cancellation. Especially, when the Hamiltonian satisfies the effective time-reversal symmetry (effective TRS),

$$\tilde{P}^\dagger H^*(\boldsymbol{k})\tilde{P} = H(-\boldsymbol{k}), \tag{18}$$

with a paraunitary matrix $\tilde{P}$, the paraunitary matrix $T(\boldsymbol{k})$ obeys the condition $T(\boldsymbol{k}) = \tilde{P}^*T^*(-\boldsymbol{k})M_{\boldsymbol{k}}$ and the Berry curvature $\Omega_{n,xy}(\boldsymbol{k})$ satisfies the relation $\Omega_{n,xy}(\boldsymbol{k}) = -\Omega_{n,xy}(-\boldsymbol{k})$ [17]. The effective TRS also imposes $E_n(\boldsymbol{k}) = E_n(-\boldsymbol{k})$ and $c_2(\rho(E_n(\boldsymbol{k}))) = c_2(\rho(E_n(-\boldsymbol{k})))$. From these, the integrand of Eq. (12) is odd in $\boldsymbol{k}$, and thus the thermal Hall conductivity $\kappa_{\alpha\beta}$ vanishes.

D. Spiral phase

To obtain nonzero thermal Hall conductivity, we need to break the effective PT and T symmetries. Here we consider AB-sublattice systems in the spiral phase and discuss the general condition for breaking the symmetries and specific examples of symmetry-breaking interactions. To this end, we consider the spin Hamiltonian

$$H = H_J + H_\Delta + H_h. \tag{19}$$

Here, the first term

$$H_J = \sum_{i\neq j} J_{\alpha\beta}(\boldsymbol{r})\boldsymbol{S}_i\cdot\boldsymbol{S}_j \tag{20}$$

denotes the Heisenberg interaction between spins $\boldsymbol{S}_i$ and $\boldsymbol{S}_j$ with the coupling $J_{\alpha\beta}(\boldsymbol{r})$, where $\alpha,\beta = A,B$ represent the sublattice to which i and j sites belong, respectively, and $\boldsymbol{r}$ represents the distance between i and j sites. The second term H_Δ is the easy-axis anisotropy part:

$$H_\Delta = \sum_i \Delta_\alpha\left(S_i^z\right)^2, \tag{21}$$

$$= \Delta_A\sum_{i\in A}\left(S_i^z\right)^2 + \Delta_B\sum_{i\in B}\left(S_i^z\right)^2. \tag{22}$$

The last term H_h is a Zeeman coupling term:

$$H_h = h\sum_i S_i^z. \tag{23}$$

We assume that the spin configuration of classical ground state is given by

$$\boldsymbol{S}_i = S(\cos\psi_i\cos(\boldsymbol{Q}\cdot\boldsymbol{R}_i+\phi_i), \cos\psi_i\sin(\boldsymbol{Q}\cdot\boldsymbol{R}_i+\phi_i), \sin\psi_i), \tag{24}$$

where $\psi_i\in[-\pi/2,\pi/2]$ describes the canting angle from the xy plane and $\boldsymbol{Q}$ represents a pitch of the spiral. The canting angle ψ_i is ψ_A (ψ_B) if i is in the A (B) sublattice. Similarly, we assume that $\phi_i = \phi_\alpha$ for $i\in\alpha$ with $\alpha = A, B$. The position $\boldsymbol{R}_i$ denotes the center of the unit cell which contains site i.

Because the spin Hamiltonian is symmetric with respect to the rotation of spin around the z axis, hereafter we set $\phi_A = 0$, $\phi_B = \phi$ without loss of generality, with which ϕ describes an in-plane angle between two spins in the same unit cell. This ansatz generally describes noncollinear spin configurations with single $\boldsymbol{Q}$.

For the present canted spins, a new spin coordinate $\boldsymbol{S}'$ along the ground-state spin configuration can be written as [24,39]

$$\boldsymbol{S}_i = R^z(\boldsymbol{Q}\cdot\boldsymbol{R}_i+\phi_i)R^y(\pi/2-\psi_i)\boldsymbol{S}'_i = \begin{pmatrix} \sin\psi_i\cos(\boldsymbol{Q}\cdot\boldsymbol{R}_i+\phi_i) & -\sin(\boldsymbol{Q}\cdot\boldsymbol{R}_i+\phi_i) & \cos\psi_i\cos(\boldsymbol{Q}\cdot\boldsymbol{R}_i+\phi_i) \\ \sin\psi_i\sin(\boldsymbol{Q}\cdot\boldsymbol{R}_i+\phi_i) & \cos(\boldsymbol{Q}\cdot\boldsymbol{R}_i+\phi_i) & \cos\psi_i\sin(\boldsymbol{Q}\cdot\boldsymbol{R}_i+\phi_i) \\ -\cos\psi_i & 0 & \sin\psi_i \end{pmatrix}\begin{pmatrix} S_i'^x \\ S_i'^y \\ S_i'^z \end{pmatrix}, \tag{25}$$

where $R^k(\theta)$ denotes a spin rotation operator with respect to the k axis by θ. Further rewriting $\boldsymbol{S}'$ with the magnon operators using Holstein-Primakoff transformation Eq. (1) and substituting it to the spin Hamiltonian Eq. (19), we obtain the 4×4 BdG Hamiltonian Eq. (4) for the present system. For the detailed form of $\Xi(\boldsymbol{k})$ and $\Pi(\boldsymbol{k})$, see Appendix.

Let us discuss the presence/absence of the effective PT symmetry for the present case. Here, for simplicity, we assume a lattice structure where the A and B sublattices are interchanged upon spatial inversion (e.g., honeycomb lattice). First, we note that the physical T and PT symmetries are explicitly broken due to the Zeeman field term H_h. However, this term is invariant under the combination of T or PT operation with π rotation of spin around the y axis. On the other hand, the ground-state spin configuration typically has a lower symmetry than the Hamiltonian, and indeed the spiral spin order is not invariant under the above symmetry operation. We here consider a symmetry operation X, which is obtained by further combining $\phi_A+\phi_B$ rotation of spin around the z axis (to the PT operation and π rotation around the y axis). The spin configuration is transformed under X as

$$\begin{aligned} &S(\cos\psi_i\cos(\boldsymbol{Q}\cdot\boldsymbol{R}_i+\phi_i), \cos\psi_i\sin(\boldsymbol{Q}\cdot\boldsymbol{R}_i+\phi_i), \sin\psi_i) \\ &\quad\to S(\cos\psi_{-i}\cos(\boldsymbol{Q}\cdot\boldsymbol{R}_i+\phi_i), \\ &\qquad \cos\psi_{-i}\sin(\boldsymbol{Q}\cdot\boldsymbol{R}_i+\phi_i), \sin\psi_{-i}), \end{aligned}$$

where $-i\in B(A)$ if $i\in A(B)$. This implies that the ground state does not change under X when $\psi_A=\psi_B$, and the magnon Hamiltonian should have a corresponding symmetry if the spin Hamiltonian is also symmetric with respect to X.

Now, let us consider how this symmetry operation X acts on the magnon Hamiltonian. To this end, first we consider the transformation for the spin operator:

$$\begin{aligned} \boldsymbol{S}_i \to X\boldsymbol{S}_i &= R^y(\pi)R^z(-\phi_A-\phi_B)(-\boldsymbol{S}_{-i}) \\ &= -R^y(\pi)R^z(-\boldsymbol{Q}\cdot\boldsymbol{R}_i-\phi_i)R^y(\pi/2-\psi_{-i})\boldsymbol{S}'_{-i}. \end{aligned}$$

On the other hand, the transformed spin operator can also be expressed using the spin coordinate along the transformed ground state $X\boldsymbol{S}'_i$ as

$$X\boldsymbol{S}_i = R^z(\boldsymbol{Q}\cdot\boldsymbol{R}_i+\phi_i)R^y(\pi/2-\psi_i)(X\boldsymbol{S}'_i).$$

In other words, when $\psi_i=\psi_{-i}$, $\boldsymbol{S}'_i$ is transformed as

$$X\boldsymbol{S}'_i = \begin{pmatrix} 1 & 0 & 0 \\ 0 & -1 & 0 \\ 0 & 0 & 1 \end{pmatrix}\boldsymbol{S}'_{-i}$$

under X. Considering the fact that only the y component $S_i'^y = i\sqrt{S/2}(\alpha_i^\dagger-\alpha_i)$ has the imaginary coefficient to the magnon operators and that the sublattices are interchanged upon spatial inversion, we can express the symmetry operation X for the magnon Hamiltonian as $H(\boldsymbol{k})\to P^\dagger H^*(\boldsymbol{k})P$ with

$$P = \begin{pmatrix} 0 & 1 & 0 & 0 \\ 1 & 0 & 0 & 0 \\ 0 & 0 & 0 & 1 \\ 0 & 0 & 1 & 0 \end{pmatrix}. \tag{26}$$

For the magnon Hamiltonian Eqs. (5) and (6), Eq. (14) is satisfied if

$$\Xi^z = \Pi^z = 0, \quad \Pi^i \in \mathbb{R}. \tag{27}$$

Let us discuss when the above condition can be broken, based on the detailed form of the magnon Hamiltonian given in the Appendix. For the Heisenberg interaction H_J, Ξ^z and Π^z are nonzero when $J_{AA}\neq J_{BB}$ [Eqs. (A3d) and (A3h)]. Furthermore, when $\psi_A\neq\psi_B$, $\mathrm{Im}\Pi^x$ and $\mathrm{Im}\Pi^y$ are also nonzero [Eqs. (A3f) and (A3g)]. For the anisotropy part H_Δ, Π^z is nonzero when $\Delta_A\neq\Delta_B$ [Eq. (A4d)]. Thus, when A sites and B sites are inequivalent, the Berry curvature can be nonzero.

Furthermore, we consider the presence/absence of the effective TRS Eq. (18), since breaking the effective TRS is necessary for nonzero thermal Hall conductivity. In particular, we focus on the simplest case of $\tilde{P}=I$ (I: an identity matrix) in the following. We need $i\cos k$ or $\sin k$ terms to break the effective TRS Eq. (18), and these terms of the BdG Hamiltonian for the spiral phase depend on $\sin(\boldsymbol{Q}\cdot R+\phi)$ or $\sin(\boldsymbol{Q}\cdot R)$. Thus, effective TRS is broken when the spin configuration satisfy $\sin(\boldsymbol{Q}\cdot R+\phi)\neq0$ or $\sin(\boldsymbol{Q}\cdot R)\neq0$. These conditions necessitate $\boldsymbol{Q}\cdot R\neq0,\pi$ or $\phi\neq0,\pi$. Hence, we need spiral configuration or nontrivial in-plane canting angle ϕ for nonzero thermal Hall conductivity besides the nonzero Berry curvature.

E. SU(2) gauge fields in magnon bands

In previous studies on thermal Hall responses of magnetic systems [14–19], the DM interaction is incorporated to generate nonzero Berry curvature of magnon bands. In this subsection, we comment on the role of the DM interaction in view of the symmetry condition [Eq. (14)] and the effective SU(2) gauge field. Specifically, we show that the presence of the DM interaction can break the symmetry Eq. (14), and discuss how the similar SU(2) gauge field is obtained without the DM interaction in the spiral phase with the sublattice inequivalence.

First, we consider the out-of-plane DM interaction

$$H_{\mathrm{DM}} = \sum_{i,j} D_{\alpha\beta}(\boldsymbol{S}_i\times\boldsymbol{S}_j)_z. \tag{28}$$

For this DM interaction, when $D_{AA} \neq D_{BB}$, we can obtain nonzero Ξ^z even if $\psi_A = \psi_B$ (see Appendix). Thus, DM interaction can break the symmetry Eq. (14) and generate the nonzero Berry curvature [19]. In addition, Ξ^z can be nonzero even if the spin configuration is the collinear and ψ_i is $\pm\pi/2$. In this case, the DM interaction can be taken into the Heisenberg coupling with a phase factor $\chi = \arctan(D/J)$,

$$J\boldsymbol{S}_i \cdot \boldsymbol{S}_j + D\boldsymbol{S}_i \times \boldsymbol{S}_j = J_{\mathrm{eff}}(e^{i\chi} S_i^+ S_j^- + e^{-i\chi} S_i^- S_j^+), \tag{29}$$

where J_{eff} is an effective Heisenberg coupling $J_{\mathrm{eff}} = \sqrt{J^2 + D^2}$. Thus, the DM interaction adds the phase factor χ to the hopping and acts as the virtual magnetic field and induce the nonzero Ξ^z.

On the other hand, in-plane DM interaction can also induce a nonzero Berry curvature with a different mechanism. The in-plane DM interaction can induce SU(2) gauge field in canted spin systems, which is a non-Abelian gauge field with respect to the sublattice degrees of freedom in the magnon representation [21]. Now, we show that we can induce the SU(2) gauge field even without the DM interaction in a system with $\psi_A \neq \psi_B$. For simplicity, we consider the antiferromagnetic Heisenberg chain with nearest-neighbor coupling:

$$H = \sum_{i\in A}(J\boldsymbol{S}_i \cdot \boldsymbol{S}_{i+1} + J'\boldsymbol{S}_i \cdot \boldsymbol{S}_{i-1}).$$

Here we assume the spiral spin configuration given by Eq. (24). Again, we can set $\phi_A = 0$ without loss of generality, and we obtain

$$\boldsymbol{S}_i = S(\cos\psi_A \cos(\boldsymbol{Q}\cdot\boldsymbol{R}_i), \cos\psi_A \sin(\boldsymbol{Q}\cdot\boldsymbol{R}_i), \sin\psi_A), \tag{30}$$

$$\begin{aligned}\boldsymbol{S}_{i+1} = {}& S(\cos\psi_B \cos(\boldsymbol{Q}\cdot\boldsymbol{R}_i + \phi),\\ &\times \cos\psi_B \sin(\boldsymbol{Q}\cdot\boldsymbol{R}_i + \phi), \sin\psi_B)\end{aligned} \tag{31}$$

for $i \in A$.

The spin Hamiltonian in the $\boldsymbol{S}'$ coordinate can be obtained with Eq. (25) as follows:

$$\begin{aligned}H = \sum_{i\in A}\big[&J_X S_i'^x S_{i+1}'^x + J_Y S_i'^y S_{i+1}'^y + J_Z S_i'^z S_{i+1}'^z\\ &+ D_0\big(S_i'^x S_{i+1}'^y - S_i'^y S_{i+1}'^x\big) + D_1\big(S_i'^x S_{i+1}'^y + S_i'^y S_{i+1}'^x\big)\\ &+ J_X' S_{i-1}'^x S_i'^x + J_Y' S_{i-1}'^y S_i'^y + J_Z' S_{i-1}'^z S_i'^z\\ &+ D_0'\big(S_{i-1}'^x S_i'^y - S_{i-1}'^y S_i'^x\big) + D_1'\big(S_{i-1}'^x S_i'^y + S_{i-1}'^y S_i'^x\big)\big],\end{aligned}$$

where

$$\begin{aligned}J_X &= J(\sin\psi_A \sin\psi_B \cos\phi + \cos\psi_A \cos\psi_B),\\ J_Y &= J\cos\phi,\\ J_Z &= J(\cos\psi_A \cos\psi_B \cos\phi + \sin\psi_A \sin\psi_B),\\ D_0 &= -J\frac{\sin\psi_A + \sin\psi_B}{2}\sin\phi,\\ D_1 &= J\frac{\sin\psi_B - \sin\psi_A}{2}\sin\phi,\\ J_X' &= J'(\sin\psi_A \sin\psi_B \cos(\phi - \boldsymbol{Q}\cdot\boldsymbol{R}) + \cos\psi_A \cos\psi_B),\\ J_Y' &= J'\cos(\phi - \boldsymbol{Q}\cdot\boldsymbol{R}),\\ J_Z' &= J'(\cos\psi_A \cos\psi_B \cos(\phi - \boldsymbol{Q}\cdot\boldsymbol{R}) + \sin\psi_A \sin\psi_B),\\ D_0' &= J'\frac{\sin\psi_A + \sin\psi_B}{2}\sin(\phi - \boldsymbol{Q}\cdot\boldsymbol{R}),\\ D_1' &= J'\frac{\sin\psi_B - \sin\psi_A}{2}\sin(\phi - \boldsymbol{Q}\cdot\boldsymbol{R}),\end{aligned}$$

with $\boldsymbol{R} = \boldsymbol{R}_{i+1} - \boldsymbol{R}_i$. In these terms, D_1 and D_1' are nonzero only when the spin configuration satisfies $\psi_A \neq \psi_B$, which implies that these are the candidates for the (effective) *PT* breaking term. Using the HP transformation Eq. (1), we can write the D_1 and D_1' terms in terms of the magnon operators as

$$\begin{aligned}&\sum_{i\in A}\frac{i}{2}[D_1(a_i^\dagger b_{i+1}^\dagger - a_i b_{i+1}) + D_1'(a_i^\dagger b_{i-1}^\dagger - a_i b_{i-1})]\\ &= \sum_{i\in A} -\frac{1}{2}\left[D_1(a_i^\dagger, b_{i+1})\sigma_y\begin{pmatrix}a_i\\ b_{i+1}^\dagger\end{pmatrix} + D_1'(a_i^\dagger, b_{i-1})\sigma_y\begin{pmatrix}a_i\\ b_{i-1}^\dagger\end{pmatrix}\right].\end{aligned}$$

Then, after the Fourier transformation, we obtain

$$\begin{aligned}\sum_k\Bigg[&-\frac{D_1 + D_1'}{4}\cos k(a_k^\dagger, b_{-k})\sigma_y\begin{pmatrix}a_k\\ b_{-k}^\dagger\end{pmatrix}\\ &- i\frac{D_1 - D_1'}{4}\sin k(a_k^\dagger, b_{-k})\sigma_y\begin{pmatrix}a_k\\ b_{-k}^\dagger\end{pmatrix}\Bigg].\end{aligned} \tag{32}$$

Here, the second term contains $i\sigma_y$ and this is the origin of the nonzero $\mathrm{Im}\Pi_y$ for the BdG Hamiltonian. This term is the same form as a Rashba spin-orbit term, since we can see $(a_k^\dagger, b_{-k})$ as a pseudospinor operator [21]. This Rashba-like term contains $D_1 - D_1'$, supporting nonzero SU(2) gauge field when $D_1 \neq D_1'$. The condition $D_1 \neq D_1'$ is satisfied when $\boldsymbol{Q}\cdot\boldsymbol{R} \neq 0, \pi$ or $J \neq J'$ and $\phi \neq 0, \pi$. Hence, we need spiral configuration or nonzero canting angle ϕ and asymmetric bonds other than the condition $\psi_A \neq \psi_B$ for the SU(2) gauge field.

In previous studies, the thermal Hall effect without DM interactions is reported in a kagome lattice system [25,26], a trimerized triangular lattice [27], and a honeycomb lattice system with $\mathrm{Im}\Pi^i = 0$ [24]. From the viewpoint of the above discussion, the nonzero Berry curvature in these previous studies is derived from the phase factor of hoppings as in the case of the out-of-plane DM interaction. In contrast, the SU(2) gauge field also induces nonzero Berry curvature as we have clarified above and demonstrate for the J_1-J_2-J_2' models in the following.

III. MAGNON HAMILTONIAN IN J_1-J_2-J_2' MODEL

Now we demonstrate the thermal Hall effect without DM interaction. As we have clarified in the above section, we need inequivalent *AB* sublattices, and $\boldsymbol{Q}\cdot R \neq 0, \pi$ or $\phi \neq 0, \pi$ for the thermal Hall effect. J_1-J_2-J_2' model on the honeycomb lattice is a simple example that satisfies above conditions. In this model, the next-nearest-neighbor coupling J_2 and J_2' induce frustration, which leads to a spiral order with $\boldsymbol{Q} \neq 0$ on the ground-state spin configuration. To make the *A* and *B* sublattices inequivalent, we introduce the inequivalent next-nearest-neighbor coupling $J_2 \neq J_2'$ or inequivalent anisotropy $\Delta_A \neq \Delta_B$.

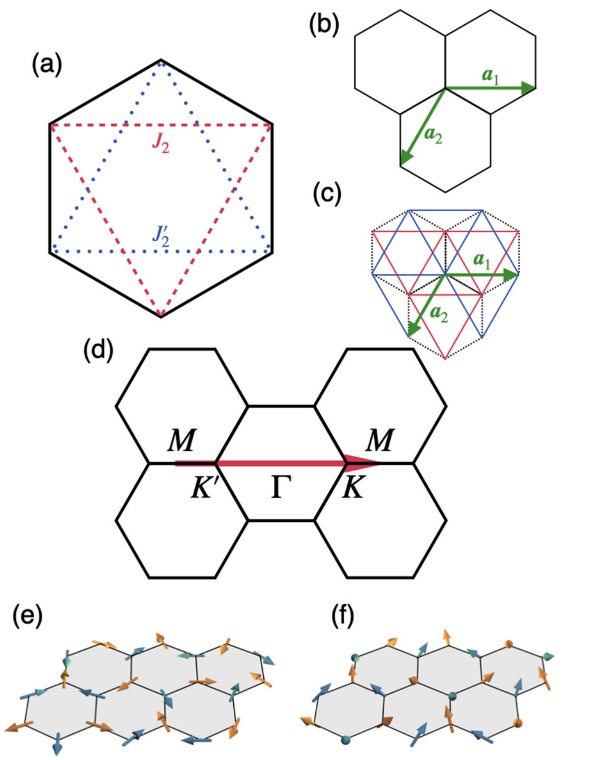

FIG. 1. (a) The J_1-J_2-J_2' model on the honeycomb lattice. (b) Vectors $\boldsymbol{a}_1$ and $\boldsymbol{a}_2$ of the honeycomb lattice. (c) Vectors $\boldsymbol{a}_1$ and $\boldsymbol{a}_2$ of bilayer triangle lattices. The red lines and blue lines each represent the top and bottom layers' triangle lattices. (d) The reciprocal space of the J_1-J_2-J_2' model on the honeycomb lattice. (e), (f) are the spin configuration of model II with $J_1 = 1.0$, $J_2 = 2.0$, $J_2' = 2.4$, $\Delta_A = \Delta_B = 0.05$. (e) $h = 0$ and the canting angle $\psi_A = \psi_B = 0$. (f) $h = 8$ and the canting angle $\psi_A \neq \psi_B$.

A. Spin Hamiltonian

We consider the Heisenberg model on the honeycomb lattice depicted in Fig. 1(a). While the honeycomb lattice has AB sublattices, we assume that these sublattices are inequivalent (e.g., composed of two different atoms), so the coupling constants may take different values for A and B sublattices, namely, here we consider the J_1-J_2-J_2' Heisenberg model, whose Hamiltonian is given by

$$H = H_J + H_\Delta + H_h, \tag{33}$$

with

$$H_J = J_1 \sum_{\langle i,j\rangle} \boldsymbol{S}_i \cdot \boldsymbol{S}_j + J_2 \sum_{\langle\langle i,j\rangle\rangle \in A} \boldsymbol{S}_i \cdot \boldsymbol{S}_j + J_2' \sum_{\langle\langle i,j\rangle\rangle \in B} \boldsymbol{S}_i \cdot \boldsymbol{S}_j, \tag{34}$$

$$H_\Delta = \Delta_A \sum_{i\in A} \left(S_i^z\right)^2 + \Delta_B \sum_{i\in B} \left(S_i^z\right)^2, \tag{35}$$

and

$$H_h = -h \sum_i S_i^z. \tag{36}$$

Here the index i runs over all sites, and $\sum_{\langle i,j\rangle}$ and $\sum_{\langle\langle i,j\rangle\rangle}$ mean the sum over the nearest neighbor and next-nearest neighbor of the honeycomb lattice, respectively. The operator $\boldsymbol{S}_i$ is a spin at site i, and A and B are sublattices of honeycomb lattice. Figure 1(b) shows the primitive lattice vectors $\boldsymbol{a}_1 = (\sqrt{3}a, 0)$ and $\boldsymbol{a}_2 = (-\sqrt{3}a/2, -3a/4)$ with the lattice constant a (Hereafter, we set $a = 1$ for simplicity), namely, A sites are located at $\boldsymbol{r} = m\boldsymbol{a}_1 + n\boldsymbol{a}_2$, while B sites are located at $\boldsymbol{r} = m\boldsymbol{a}_1 + n\boldsymbol{a}_2 + (0, a)$. Figure 1(d) shows the reciprocal space of the J_1-J_2-J_2' model on the honeycomb lattice.

We note that this model can also be regarded as a bilayer triangular lattice system by considering A (B) sites as the top (bottom) layer [see Fig. 1(c)]. In this case, $\sum_{\langle i,j\rangle}$ and $\sum_{\langle\langle i,j\rangle\rangle}$ indicate sums over nearest-neighbor interlayer and intralayer couplings, respectively. In particular, we emphasize that it is not necessarily unrealistic to consider a situation where J_2 and J_2' are much larger than J_1.

In the case of $h = 0$ and $J_2 = J_2'$, the classical limit of this model is studied. If $J_2/J_1 > 1/6$, the ground-state spin configuration is given as [40–44]

$$\boldsymbol{S}_i = S(\cos(\boldsymbol{Q}\cdot\boldsymbol{R}_i), \sin(\boldsymbol{Q}\cdot\boldsymbol{R}_i), 0) \quad \text{for } i \in A, \tag{37}$$

$$\boldsymbol{S}_i = S(\cos(\boldsymbol{Q}\cdot\boldsymbol{R}_i + \phi), \sin(\boldsymbol{Q}\cdot\boldsymbol{R}_i + \phi), 0) \quad \text{for } i \in B. \tag{38}$$

In the spiral phase, we can minimize the classical energy by taking

$$\boldsymbol{Q} = \left(\frac{2}{\sqrt{3}a}\cos^{-1}\left(\frac{J_1 - 2J_2}{4J_2}\right), 0, 0\right), \tag{39}$$

$$\phi = \pi. \tag{40}$$

We note here that there are two other ground states rotated by $\pm\frac{2\pi}{3}$ in the honeycomb plane.

In the case of $h \neq 0$ and $J_2 \neq J_2'$, we assume that classical ground states can be written as Eq. (24). Even for $J_2 \neq J_2'$, we assume $\phi_A = 0$ and $\phi_B = \pi$, which is the known result for the $J_2 = J_2'$ case [42], namely, we write the classical ground states as

$$\boldsymbol{S}_i = S(\cos\psi_A \cos(\boldsymbol{Q}\cdot\boldsymbol{R}_i), \cos\psi_A \sin(\boldsymbol{Q}\cdot\boldsymbol{R}_i), \sin\psi_A) \quad \text{for } i \in A, \tag{41}$$

$$\boldsymbol{S}_i = S(-\cos\psi_B \cos(\boldsymbol{Q}\cdot\boldsymbol{R}_i), -\cos\psi_B \sin(\boldsymbol{Q}\cdot\boldsymbol{R}_i), \sin\psi_B) \quad \text{for } i \in B. \tag{42}$$

Here, ψ_A and ψ_B are canting angles from the xy plane, and we estimate $\boldsymbol{Q}$, ψ_A, and ψ_B by minimizing the classical energy

$$\begin{aligned} E =& NS^2[-J_1 \cos\psi_A \cos\psi_B(1 + \cos(Q_1 + Q_2) + \cos Q_2) \\ &+ (J_2 \cos^2\psi_A + J_2' \cos^2\psi_B) \\ &\times (\cos Q_1 + \cos Q_2 + \cos(Q_1 + Q_2)) \\ &+ 3J_1 \sin\psi_A \sin\psi_B + 3(J_2 \sin^2\psi_A + J_2' \sin^2\psi_B) \\ &+ \Delta_A \sin^2\psi_A + \Delta_B \sin^2\psi_B] \\ &- NS(h \sin\psi_A + h \sin\psi_B), \end{aligned} \tag{43}$$

where N is the site number of A and B sites, and $Q_1 = \sqrt{3}aQ_x$, $Q_2 = -\sqrt{3}a/2Q_x - 3a/4Q_y$. For the case of $h = 0$, due to the (easy-plane) magnetic anisotropy, the canting angles ψ_A and ψ_B are zero. Figure 1(e) shows the spin configuration of this

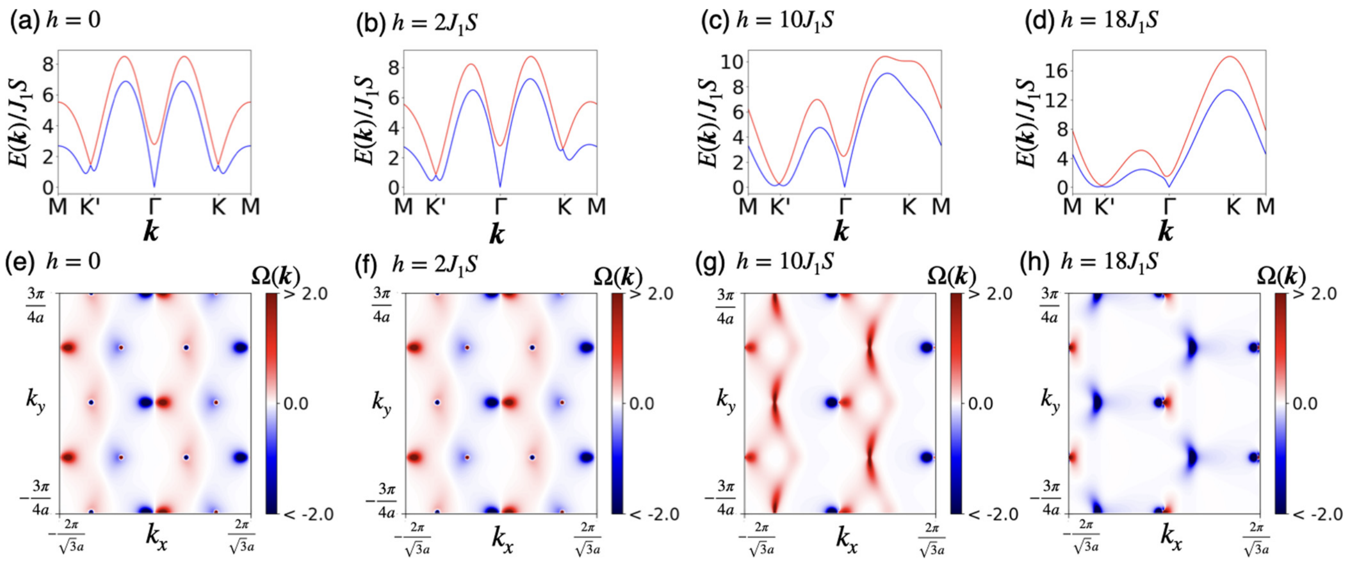

FIG. 2. The energy band and the Berry curvature Ω_{xy} of the model I with $J_1 = 1.0$, $J_2 = 2.0$, $J_2' = 2.4$, $\Delta_A = \Delta_B = 0.05$. (a)–(d) The energy bands for (a) $h = 0$, (b) $h = 2J_1S$, (c) $h = 10J_1S$, and (d) $h = 18J_1S$. (e)–(h) The Berry curvature Ω_{xy} of the lower band for (e) $h = 0$, (f) $h = 2J_1S$, (g) $h = 10J_1S$, and (h) $h = 18J_1S$.

case. When $h > 0$, on the other hand, spins are canted from the xy plane as shown in Fig. 1(f).

B. Magnon band, Berry curvature, and Chern number

We apply Holstein-Primakoff transformation for the spin Hamiltonian Eq. (33) and obtain the magnon Hamiltonian (for details, see Appendix). In this model, there are two types of inequivalence introduced by (I) inequivalent Heisenberg coupling for two triangular lattices ($J_2 \neq J_2'$) and (II) inequivalent anisotropy for two triangular lattices ($\Delta_A \neq \Delta_B$). Thus we name model I $J_2 \neq J_2'$, $\Delta_A = \Delta_B$ and model II $J_2 = J_2'$, $\Delta_A \neq \Delta_B$. In the following, we first discuss the results for model I with $J_2 \neq J_2'$, and then proceed to the results for model II with $\Delta_A \neq \Delta_B$.

In Fig. 2, we show the energy band and the Berry curvature of model I, which has inequivalent Heisenberg coupling for two triangular lattices ($J_2 \neq J_2'$). Here, the energy band is plotted along the paths shown in Fig. 1(d).

Figures 2(a) and 2(e) show the energy band and the Berry curvature in the absence of the external magnetic field, $h = 0$. From Fig. 2(a), we can see that the small gaps around K and K' are energetically equivalent to each other. In this case, band gaps open, and the Berry curvature is nonzero as shown in Fig. 2(e), although the thermal Hall conductivity vanishes because the magnon Hamiltonian satisfies the effective TRS $H^*(\boldsymbol{k}) = H(-\boldsymbol{k})$.

We show the energy band of model I ($J_2 \neq J_2'$) with magnetic field $h = 2J_1S$, $h = 10J_1S$, and $h = 18J_1S$ in Figs. 2(b)–2(d), respectively. If we turn on the magnetic field $h \neq 0$, the two small gaps around K and K' points become energetically inequivalent, since the effective TRS is now broken [$H(\boldsymbol{k}) \neq H^*(-\boldsymbol{k})$]. Figures 2(b)–2(d) show that the energy around K' decreases when $h \neq 0$ and energy around K increases. These changes in the band structure produce changes in the Berry curvature.

Figures 2(f)–2(h) show the Berry curvature with $h = 2J_1S$, $h = 10J_1S$, and $h = 18J_1S$. In the $h = 2J_1S$ case, the Berry curvature satisfies $\Omega_{n,xy}(\boldsymbol{k}) \simeq -\Omega_{n,xy}(-\boldsymbol{k})$ similarly to the $h = 0$ case, as one can see from Fig. 2(f). As shown in Figs. 2(c) and 2(d), as the magnetic field increases, the gap around K becomes larger and, accordingly, the Berry curvature around K becomes smaller as shown in Figs. 2(g) and 2(h).

From magnetic-field dependence of Berry curvatures, we can predict that the Chern number is zero when the magnetic field is small, while the nonzero Chern number is realized for larger h. We show the magnetic-field dependence of the Chern number and the thermal Hall conductivity in Fig. 3(a). From the upper figure of Fig. 3(a), we see that the Chern number is nonzero when the magnetic field h is large. The lower panel of Fig. 3(a) shows the color plot of the thermal Hall conductivity, while Fig. 3(b) shows the thermal Hall conductivity at several temperatures. While the thermal Hall conductivity is related to the Berry curvature via Eq. (12), unlike the Hall effect of electron systems, the thermal Hall effect of magnons is not quantized because the function $c_2(\rho(E)$ in Eq. (12) is not the function like a step function. Nonetheless, the thermal Hall conductivity shows a behavior related to that of the Chern number. To see this, first we remark that the Berry curvature of the upper band $\Omega_{1,\alpha\beta}$ and the lower band $\Omega_{2,\alpha\beta}$ satisfies $\Omega_{1,\alpha\beta} \sim -\Omega_{2,\alpha\beta}$, and that $-(c_2(\rho(E)) - \frac{\pi^2}{3})$ in Eq. (12) is a monotonously increasing function. These imply that the sign of the thermal Hall conductivity corresponds to the sign of the Chern number of the upper band. Especially, Figs. 3(a) and 3(b) show that the sign of the thermal Hall conductivity changes reflecting the sign change of the Chern number.

The thermal Hall effect also appears in model II, which has inequivalent anisotropy for two triangular lattices ($\Delta_A \neq \Delta_B$) in a similar way to model I ($J_2 \neq J_2'$) with some changes in details. We show the energy band of $h = 0$, $h = 8J_1S$, $h = 12J_1S$, and $h = 20J_1S$ in Figs. 4(a)–4(d), and the Berry

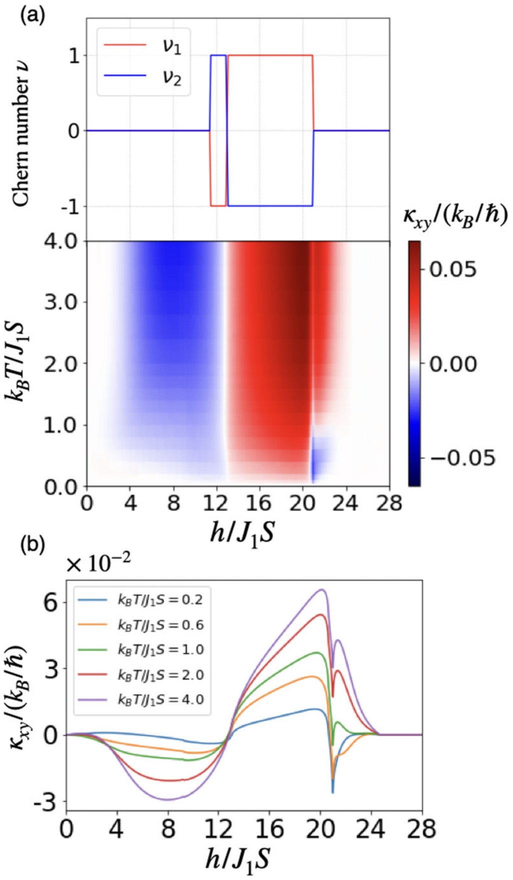

FIG. 3. The Chern number ν and the thermal Hall conductivity κ_{xy} of the model I with $J_1 = 1.0$, $J_2 = 2.0$, $J_2' = 2.4$, $\Delta_A = \Delta_B = 0.05$. Here, we calculate κ_{xy} with $S = \frac{1}{2}$. (a) The magnetic field dependence of ν for each magnon band and the color plot of κ_{xy}. ν_1 is the Chern number of the upper band and ν_2 is the Chern number of the lower band. The lower panel is the color plot of κ_{xy}. The sign of κ_{xy} almost coincides with the sign of ν_1. In particular, κ_{xy} becomes zero and shows a sign change around $h \sim 13J_1S$, where the sign of ν_1 changes. (b) κ_{xy} plotted as a function of the magnetic field for several temperatures.

curvature of $h = 0$, $h = 8J_1S$, $h = 12J_1S$, and $h = 20J_1S$ in Figs. 4(e)–4(h). When the magnetic field is zero, the Hamiltonian satisfies the effective TRS. Thus, the Berry curvature $\Omega_{n,xy}(\boldsymbol{k})$ satisfies $\Omega_{n,xy}(\boldsymbol{k}) = -\Omega_{n,xy}(-\boldsymbol{k})$ as shown in Figs. 4(e), and the thermal Hall conductivity is zero, as in model I ($J_2 \neq J_2'$). Figures 4(b)–4(d) show that the energy around K' decreases when $h \neq 0$ while energy around K increases, which is the same as model I ($J_2 \neq J_2'$). We show the magnetic-field dependence of the Chern number and the color plot of thermal Hall conductivity in Fig. 5(a). Figure 5(b) shows the thermal Hall conductivity in some temperatures. The sign of the thermal Hall conductivity changes near the magnetic fields $h \sim 9$ and $h \sim 18$. They are not directly associated with the behavior of the Chern number as the Chern number does not show a sign change in model II ($\Delta_1 \neq \Delta_2$), contrasting to the case of model I ($J_2 \neq J_2'$), where the sign change of κ and ν takes place at almost the same h. Specifically, around $h \sim 9$, we can see in Figs. 4(f) and 4(g) that positive contributions of the Berry curvature appear around the K' point as increasing h, which cause a sign change of the thermal Hall conductivity. Around $h \sim 18$, the sign change of the thermal Hall conductivity reflects the Berry curvature around the Γ point where the energy gap becomes small. Since the sign changes of the thermal Hall conductivity around $h \sim 9$ and $h \sim 18$ are not accompanied by a sign change of the Chern number, the magnetic field h where κ changes its sign shows a large temperature dependence, as opposed to those associated with the sign change of the Chern number in model I ($J_2 \neq J_2'$). Instead, the Chern number change at $h \sim 19$ gives rise to an abrupt jump of the thermal Hall conductivity at all temperatures as seen in Fig. 5(b).

We note that our assumption for the ground state spin configuration Eq. (24) becomes not so good in the large magnetic field region. While Figs. 3(b) and 5(b) show that the thermal Hall conductivity changes dramatically about $h = 21J_1S$, this region may be out of validity of our ansatz Eq. (24) because $\psi_A = \pi/2$ and $\psi_B < \pi/2$ in this region. Specifically, when $\psi_A = \pi/2$ and $\psi_B < \pi/2$, the classical energy is independent of the angle $\boldsymbol{Q} \cdot \boldsymbol{R}_i$ of the A-site spins and the in-plane angle of the A-site spins becomes arbitrary.

IV. SPIN NERNST EFFECT

In this section, we study spin current response induced by thermal gradient in frustrated honeycomb magnets. In particular, we consider a transverse response called the spin Nernst effect.

Because the spin Hamiltonian described as Eq. (33) commutes with S^z, we can define spin current. However, a problem arises when we approximate spin Hamiltonian as a bilinear form of creation and annihilation operators of the magnon, especially when we consider noncollinear systems. Specifically the magnon Hamiltonian itself does not commute with spin operator S^z. In noncollinear systems, the spin operator S^z is written by the $\boldsymbol{S}'$ as Eq. (25), and S^z is not a bilinear form of magnon operators unlike collinear systems. Thus, in the noncollinear systems, the commutation of S^z and the magnon Hamiltonian changes the order of creation and annihilation operators of magnons. To overcome this issue, we use a formulation of current associated with a general operator before considering the spin operator. Specifically, we write the general operator on the magnon space as

$$O(\boldsymbol{r}) = \tfrac{1}{2}\Psi^\dagger(\boldsymbol{r})O\Psi(\boldsymbol{r}).$$

Here, Ψ is defined as Eq. (3) and O is the 4×4 matrix. Thus, we can write the time differential of $O(\boldsymbol{r})$ as the current $\boldsymbol{j}_o$ part and source S_o part [5,35],

$$\frac{\partial O(\boldsymbol{r})}{\partial t} = i[H, O(\boldsymbol{r})] = -\nabla \cdot \boldsymbol{j}_o + S_o, \tag{44}$$

where $\boldsymbol{j}_o = \frac{1}{4}(O\sigma_3\boldsymbol{v} + \boldsymbol{v}\sigma_3 O)$, $S_o = -\frac{i}{2}(O\sigma_3 H(\boldsymbol{k}) - H(\boldsymbol{k})\sigma_3 O)$, and $\boldsymbol{v} = i[H(\boldsymbol{k}), \boldsymbol{r}]$. In the case of collinear antiferromagnets, $S^z\sigma_3 = 1$ and S_o disappears, and $\boldsymbol{j}_o$ clearly describes the spin current. In our model, $S_o \neq 0$ because we consider noncollinear systems, but we still adopt J_o as a definition of the spin current, following the discussions in Ref. [35].

Hereafter, we focus on the spin Nernst effect and we set O to be $\tilde{S}^z$, which corresponds to the magnon spin density

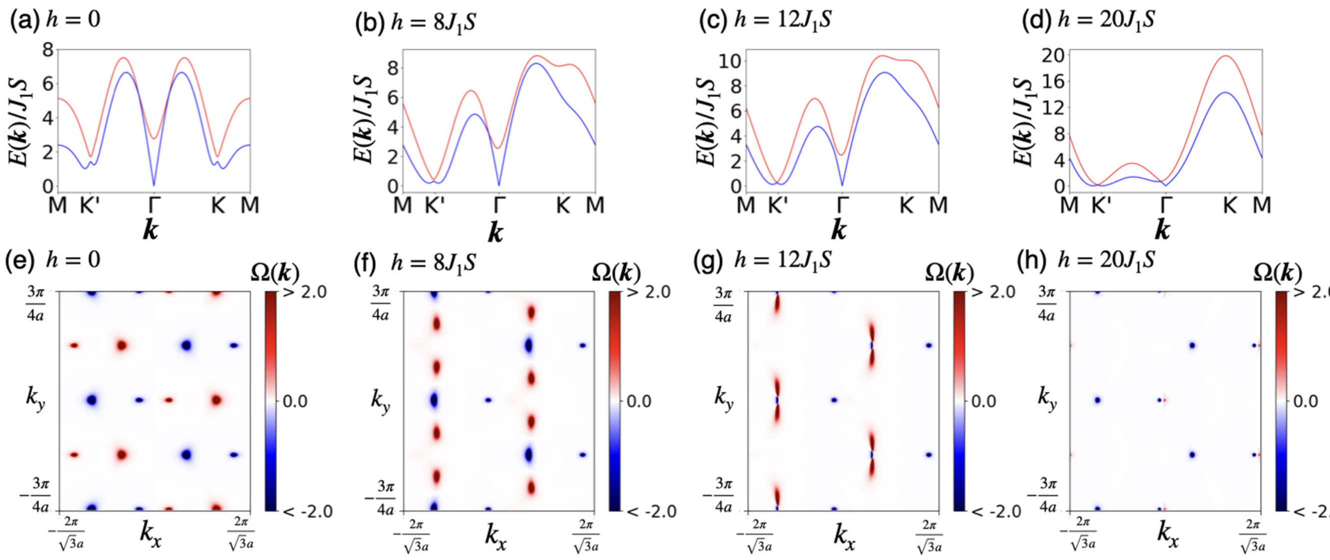

FIG. 4. The energy band and the Berry curvature Ω_{xy} of model II with $J_1 = 1.0$, $J_2 = J_2' = 2.0$, $\Delta_A = 0.05$, $\Delta_B = 0.1$. (a)–(d) is the energy band (a) at $h = 0$, (b) at $h = 8J_1S$, (c) at $h = 12J_1S$, and (d) at $h = 20J_1S$. (e)–(h) show the Berry curvature of the lower band (e) at $h = 0$, (f) at $h = 8J_1S$, (g) at $h = 12J_1S$, and (h) at $h = 20J_1S$. The Berry curvature Ω_{xy} is large where the energy gap is small.

operator given by

$$\tilde{S}^z = \begin{pmatrix} \sin\psi_A & 0 & 0 & 0 \\ 0 & \sin\psi_B & 0 & 0 \\ 0 & 0 & \sin\psi_A & 0 \\ 0 & 0 & 0 & \sin\psi_B \end{pmatrix}.$$

Using the linear response theory for $\boldsymbol{j}$, we obtain the expression for the spin Nernst effect as [35]

$$\begin{aligned} j_\mu &= \alpha_{\mu\nu}\nabla_\nu T \\ &= \frac{2k_B}{\hbar}\sum_n \int_{\mathrm{BZ}} \frac{dk^2}{(2\pi)^2}[\Omega^{S_z}(\boldsymbol{k})]_{n,\mu\nu} c_1(\rho(E_n(\boldsymbol{k}))\nabla_\beta T, \end{aligned} \quad (45)$$

where

$$\begin{aligned} &[\Omega^{S_z}(\boldsymbol{k})]_{n,\mu\nu} \\ &\quad = \sum_{m\neq n}(\sigma_3)_{nn}(\sigma_3)_{mm} \\ &\qquad \times \frac{2\mathrm{Im}[\langle \boldsymbol{t}_n(\boldsymbol{k})|j_\mu(\boldsymbol{k})|\boldsymbol{t}_m(\boldsymbol{k})\rangle\langle \boldsymbol{t}_m(\boldsymbol{k})|v_\nu(\boldsymbol{k})|\boldsymbol{t}_n(\boldsymbol{k})\rangle]}{[(\sigma_3 E(\boldsymbol{k}))_{nn} - (\sigma_3 E(\boldsymbol{k}))_{mm}]^2} \end{aligned} \quad (46)$$

and

$$c_1(\rho) = (1+\rho)\ln(1+\rho) - \rho\ln\rho.$$

While the formula for spin Nernst conductivity does not contain the Berry curvature, breaking of the symmetry Eq. (14) is also needed for the nonzero spin Nernst conductivity. Specifically, if A and B sites are equivalent and the symmetry Eq. (14) is satisfied, we have $Pv_\mu(\boldsymbol{k})P = P\frac{\partial H(\boldsymbol{k})}{\partial k_\mu}P = v_\mu^*(\boldsymbol{k})$ and $Pj_\mu(\boldsymbol{k})P = j_\mu^*(\boldsymbol{k})$. Thus, similarly to the Berry curvature, Ω^{S_z} must be odd in $\boldsymbol{k}$, $\Omega^{S_z}(\boldsymbol{k})_{\mu\nu,n} = -\Omega^{S_z}(-\boldsymbol{k})_{\mu\nu,n}$.

Figure 6(a) shows the color plot of the spin Nernst conductivity for model I ($J_2 \neq J_2'$), and Fig. 6(c) shows that for model II ($\Delta_A \neq \Delta_B$). These figures show that the sign of the spin Nernst conductivity is approximately corresponding to the sign of the thermal Hall conductivity. Figures 6(b) and 6(d) show the spin Nernst conductivity for model I ($J_2 \neq J_2'$) and model II ($\Delta_A \neq \Delta_B$) at several temperatures, respectively. In both cases, the spin Nernst conductivity is small when the magnetic field h is small. This is because $\langle S^z\rangle$ is small for a small magnetic field h. Since the spin Nernst effect in the present model requires nonzero $\langle S^z\rangle$, small h leads to small spin Nernst effect through its dependence on $\langle S^z\rangle$. On the other hand, when the magnetic field h/J_1S is large, the behavior of the spin Nernst conductivity resembles that of the thermal Hall conductivity. While we can see a drastic change in the spin Nernst conductivity in the large magnetic field regime $h > 20J_1S$, the ansatz Eq. (24) is not reasonable as we have mentioned in Sec. III.

Finally, we show the edge modes of the magnon band. We impose a periodic boundary condition to the x direction and an open boundary condition to the y direction. This choice of the boundary results in the zigzag edge. Figure 7(a) shows the energy dispersion of the case when the A and B sites are equivalent ($J_2 = J_2'$ and $\Delta_A = \Delta_B$), and Fig. 7(b) shows the case when the A sites and the B sites are inequivalent ($J_2 \neq J_2'$). The band structures show that only when the A and B sites are inequivalent, the edge modes appearing at the opposite edges (red and blue lines) are energetically nondegenerate. Thus, when the A and B sites are inequivalent, two edge states are inequivalent and allow transverse responses of heat and spins.

V. DISCUSSIONS

We have established the condition of the magnon thermal Hall effect without DM interaction in terms of the symmetry of the BdG Hamiltonian. The symmetry argument shows that the Berry curvature is nonzero when the A and B sites are inequivalent. Furthermore, the canting angle from xy plane ψ_A and ψ_B can induce the SU(2) gauge field when $\psi_A \neq \psi_B$.

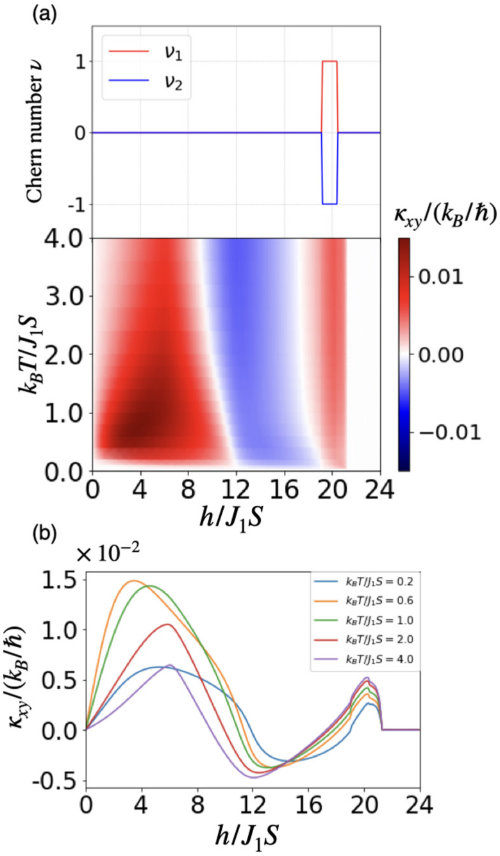

FIG. 5. The Chern number ν and the thermal Hall conductivity κ_{xy} of model II with $J_1 = 1.0$, $J_2 = J_2' = 2.0$, $\Delta_A = 0.05$, $\Delta_B = 0.1$. Here, we calculate κ_{xy} with $S = \frac{1}{2}$. (a) The magnetic field dependence of ν for each magnon band and the color plot of the thermal Hall conductivity. ν_1 is the Chern number of the upper band and ν_2 is the Chern number of the lower band. κ_{xy} becomes zero and shows a sign change around $h \sim 18J_1S$, where the Chern number ν changes. (b) The thermal Hall conductivity plotted as the function of the magnetic field for several temperatures.

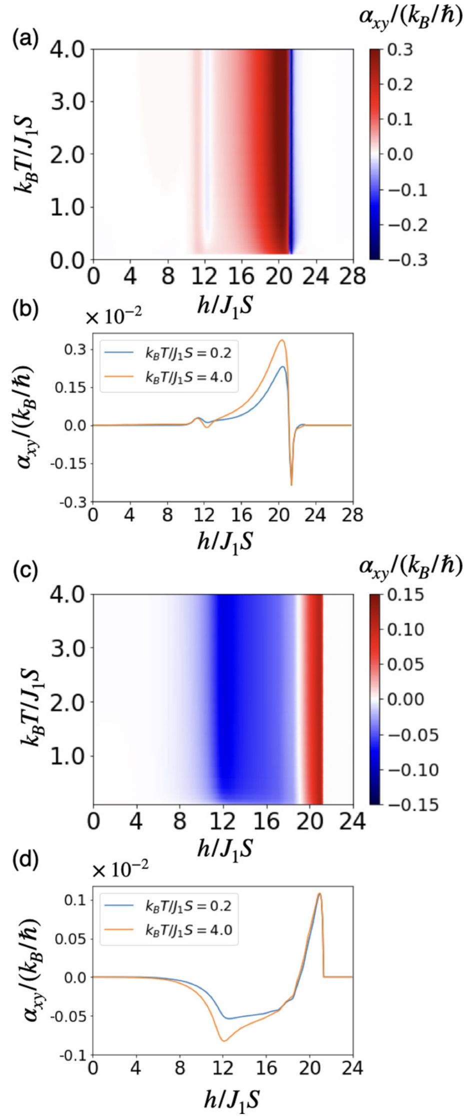

FIG. 6. The spin Nernst conductivity. (a), (b) The spin Nernst conductivity α_{xy} of model I with $J_1 = 1.0$, $J_2 = 2.0$, $J_2' = 2.2$, $\Delta_A = \Delta_B = 0.05$, $S = \frac{1}{2}$. (a) α_{xy} as a function of the magnetic field at several temperatures and (b) the color plot of α_{xy} for model I. (c), (d) The spin Nernst conductivity α_{xy} of model II with $J_1 = 1.0$, $J_2 = J_2' = 2.0$, $\Delta_A = 0.05$, $\Delta_B = 0.1$. (c) α_{xy} as a function of the magnetic field at several temperatures and (d) the color plot of α_{xy} for model II. (c), (d) indicate that the sign of the spin Nernst conductivity α_{xy} approximately corresponds to the sign of the thermal Hall conductivity.

We also study the J_1-J_2-J_2' model to clarify the relation of the thermal Hall conductivity and the Chern number.

Here, we consider materials such that the J_1-J_2-J_2' model on the honeycomb lattice is feasible. Since we set the parameter $J_2 > J_1$ in Sec. III, we can regard the J_1-J_2-J_2' model on the honeycomb lattice as the bilayer triangular lattice. One of the candidate materials of antiferromagnetic Heisenberg model on the triangular lattice is $Ba_3XSb_2O_9$ (X = Mn, Co, and Ni) [45–51]. The materials $Ba_3XSb_2O_9$ contain a stacked triangular lattice, but these layers are equivalent. Thus, we need to add inequivalence to each layer, for example, by adding an electric field in the direction of the c axis. Another candidate material is TMD. In particular, numerical calculations suggest that the ground state of VX_2 and MnX_2 (X = Cr, Br, and I) has a 120° antiferromagnetic spin configurations [52]. Thus, we may create a J_1-J_2-J_2' model by heterostacking VX_2 and MnX_2.

Let us estimate the thermal Hall conductivity in units of W/Km, with the estimated interlayer distance $d \sim 14$ Å and intralayer coupling $J_2/k_B \sim 18$ K for $Ba_3CoSb_2O_9$ [45,46]. By using these parameters and assuming $J_1 \sim J_2/2$ and the temperature $k_BT \sim 2J_1 \sim J_2$, the unit of the thermal Hall conductivity $\kappa_{xy}/(k_B/\hbar)$ approximately corresponds to $\kappa_{xy} \sim 0.03$ W/Km. Therefore, the order of the thermal Hall conductivity is 10^{-3} W/Km in our models. Experimentally, the thermal Hall conductivity $\kappa \sim 10^{-3}$ W/Km has been observed from magnons in an insulating ferromagnet with a pyrochlore lattice structure [9]. Thus, the proposed thermal Hall conductivity in this paper is feasible for experimental detection.

Finally, we comment on models other than the J_1-J_2-J_2' model on the honeycomb lattice, where the thermal Hall effect may occur without DM interaction. One candidate is the

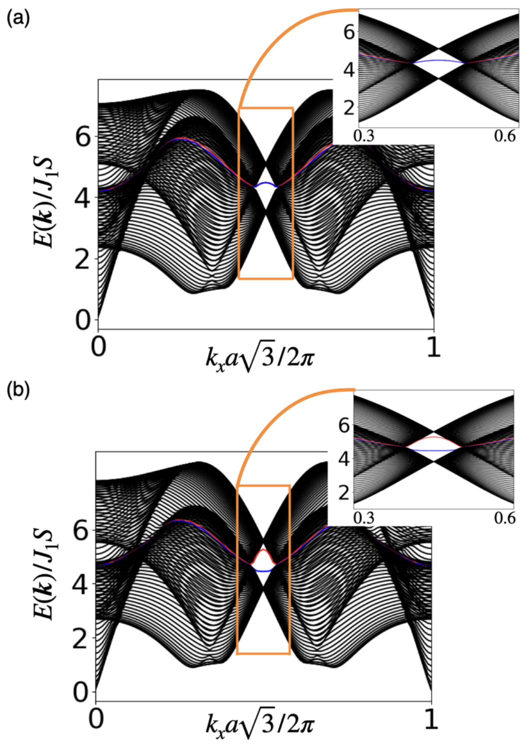

FIG. 7. The energy dispersion of zigzag edge with $J_1 = 1.0$, $h = 0$. The red and blue line is edge modes. (a) The energy dispersion of the AB equivalent model, $J_2 = J_2' = 2.0$, $\Delta_A = \Delta_B = 0.05$. (b) The energy dispersion and edge modes of model II, $J_2 = 2.0$, $J_2' = 2.2$, $\Delta_A = \Delta_B = 0.05$. Insets of (a) and (b) show the energy dispersion around the edge. In (b), the edge modes are energetically separable, while the edge modes are degenerate in (a).

J_1-J_2-J_3 model on the square lattice (as illustrated in Fig. 8) whose classical ground state exhibits a spiral phase [53–58]. The square lattice is a bipartite lattice and we can define A and B sites. To support nonzero thermal Hall response, the inequivalence of two sublattices can be introduced by changing the magnetic anisotropy or next-nearest-neighbor hopping of A and B sites. This leads to the Hamiltonian written as

$$H = \sum_{\langle i,j\rangle} J_1 \boldsymbol{S}_i \cdot \boldsymbol{S}_j + \sum_{\langle\langle i,j\rangle\rangle \in A} J_2 \boldsymbol{S}_i \cdot \boldsymbol{S}_j + \sum_{\langle\langle i,j\rangle\rangle \in B} J_2' \boldsymbol{S}_i \cdot \boldsymbol{S}_j + \sum_{\langle\langle\langle i,j\rangle\rangle\rangle \in A} J_3 \boldsymbol{S}_i \cdot \boldsymbol{S}_j + \sum_{\langle\langle\langle i,j\rangle\rangle\rangle \in B} J_3' \boldsymbol{S}_i \cdot \boldsymbol{S}_j + \sum_{i\in A} \Delta_A \left(S_i^z\right)^2 + \sum_{i\in B} \Delta_B \left(S_i^z\right)^2 + h\sum_i S_i^z,$$

where $\sum_{\langle\langle\langle i,j\rangle\rangle\rangle}$ means that sum over third-nearest neighbor of the square lattice. In this model, $J_2 \neq J_2'$ or $J_3 \neq J_3'$ or $\Delta_A \neq \Delta_B$ will support the nonzero Berry curvature and thermal Hall responses.

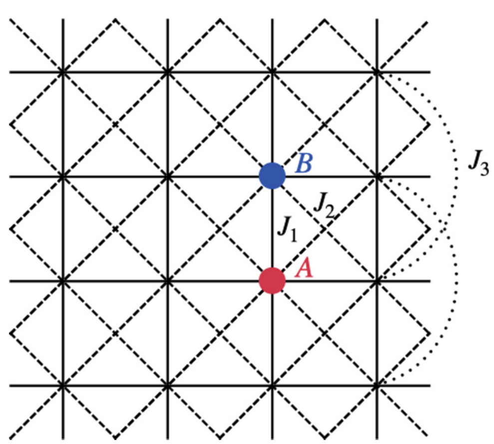

FIG. 8. The J_1-J_2-J_3 model on the square lattice. Solid, dashed, and dotted lines represent J_1, J_2, and J_3, respectively. For visibility, the third-nearest-neighbor hopping J_3 is depicted only partially on the right edge.

ACKNOWLEDGMENTS

We thank Shuichi Murakami for fruitful discussions. This work was supported by JSPS KAKENHI Grant No. 20K14407 (S.K.), JST CREST (Grant No. JPMJCR19T3) (S.K., T.M.), and JST PRESTO (Grant No. JPMJPR19L9) (T.M.). K.F. was supported by the Forefront Physics and Mathematics program to drive transformation (FoPM).

APPENDIX: DETAILS OF THE MAGNON HAMILTONIAN IN THE SPIRAL PHASE

In this Appendix, we show details of the calculation of the magnon Hamiltonian Eq. (19) in the spiral phase and identify the symmetry-breaking interactions based on the condition Eq. (27) leading to the effective PT symmetry.

First, we rewrite the spin Hamiltonian Eq. (19) in the rotated spin coordinate Eq. (25) as

$$\begin{aligned} H = \sum_{i,j} J_{\alpha\beta} \big[&(\sin\psi_i \sin\psi_j \cos\theta_{ij} + \cos\psi_i \cos\psi_j) S_i'^x S_j'^x \\ &+ \cos\theta_{ij} S_i'^y S_j'^y + (\cos\psi_i \cos\psi_j \cos\theta_{ij} \\ &+ \sin\psi_i \sin\psi_j) S_i'^z S_j'^z \\ &- \sin\psi_i \sin\theta_{ij} S_i'^x S_j'^y + \sin\psi_j \sin\theta_{ij} S_i'^y S_j'^x\big] \\ &+ \sum_i \left[h \sin\psi_\alpha S_i'^z + \Delta_\alpha \left(\cos^2\psi_i (S_i'^x)^2 + \sin^2\psi_i (S_i'^z)^2\right)\right] \\ &+ \left(S_i'^x S_j'^z \text{ and } S_i'^y S_j'^z \text{ terms}\right), \end{aligned} \tag{A1}$$

where $\alpha, \beta = A, B$ denote the sublattices to which i and j sites belong, respectively, and $\theta_{ij} = \boldsymbol{Q}\cdot\boldsymbol{R}_j + \phi_j - \boldsymbol{Q}\cdot\boldsymbol{R}_i - \phi_i$. To this Hamiltonian Eq. (A1), we apply the HP transformation Eq. (1) and obtain the magnon Hamiltonian in the form of

$$H(\boldsymbol{k}) = H_0 + \sum_{\boldsymbol{R}} H(\boldsymbol{k}, \boldsymbol{R}, \boldsymbol{r}). \tag{A2}$$

Here, H_0 consists of the local terms, i.e., the easy-axis anisotropy and the Zeeman term, while $H(\boldsymbol{k}, \boldsymbol{R}, \boldsymbol{r})$ represents the Heisenberg interaction part. The vector $\boldsymbol{R}$ denotes the distance between centers of unit cells $\boldsymbol{R}_j - \boldsymbol{R}_i$ and the summation is taken over all the unit cells (with fixing $\boldsymbol{R}_i$ at the origin). The vector $\boldsymbol{r}$ is a short-hand notation for the distance between i site and j site, and takes $\boldsymbol{r} = \boldsymbol{R}$ for the diagonal part (e.g., Ξ^0 and Ξ^z) and $\boldsymbol{r} = \boldsymbol{R} + \boldsymbol{\delta}$ for the off-diagonal part (e.g., Ξ^x and

Ξ^y) of 2×2 blocks in the following, where $\boldsymbol{\delta}$ is defined as a distance from the A site to the B site in the same unit cell.

Let us write the magnon Hamiltonian $H(\boldsymbol{k},\boldsymbol{R},\boldsymbol{r})$ as

$$H(\boldsymbol{k},\boldsymbol{R},\boldsymbol{r}) = \begin{pmatrix} \Xi(\boldsymbol{k},\boldsymbol{R},\boldsymbol{r}) & \Pi(\boldsymbol{k},\boldsymbol{R},\boldsymbol{r}) \\ \Pi^*(-\boldsymbol{k},\boldsymbol{R},\boldsymbol{r}) & \Xi^*(-\boldsymbol{k},\boldsymbol{R},\boldsymbol{r}) \end{pmatrix}.$$

Using Pauli matrices, we expand $\Xi(\boldsymbol{k},\boldsymbol{R},\boldsymbol{r})$ and $\Pi(\boldsymbol{k},\boldsymbol{R},\boldsymbol{r})$ as

$$\begin{aligned}\Xi(\boldsymbol{k},\boldsymbol{R},\boldsymbol{r}) &= \Xi^0(\boldsymbol{k},\boldsymbol{R},\boldsymbol{r})\sigma_0 + \Xi^x(\boldsymbol{k},\boldsymbol{R},\boldsymbol{r})\sigma_x \\ &\quad + \Xi^y(\boldsymbol{k},\boldsymbol{R},\boldsymbol{r})\sigma_y + \Xi^z(\boldsymbol{k},\boldsymbol{R},\boldsymbol{r})\sigma_z, \\ \Pi(\boldsymbol{k},\boldsymbol{R},\boldsymbol{r}) &= \Pi^0(\boldsymbol{k},\boldsymbol{R},\boldsymbol{r})\sigma_0 + \Pi^x(\boldsymbol{k},\boldsymbol{R},\boldsymbol{r})\sigma_x \\ &\quad + \Pi^y(\boldsymbol{k},\boldsymbol{R},\boldsymbol{r})\sigma_y + \Pi^z(\boldsymbol{k},\boldsymbol{R},\boldsymbol{r})\sigma_z.\end{aligned}$$

From the symmetry analysis, we show that nonzero $\Xi^z(\boldsymbol{k},\boldsymbol{R},\boldsymbol{r})$, $\Pi^z(\boldsymbol{k},\boldsymbol{R},\boldsymbol{r})$, or $\mathrm{Im}\Pi^i(\boldsymbol{k},\boldsymbol{R},\boldsymbol{r})$ may lead to the nonzero Berry curvature [see Eq. (27)]. Here, each coefficient of the Pauli matrices for Ξ is given as follows:

$$\begin{aligned}\Xi^0&(\boldsymbol{k},\boldsymbol{R},\boldsymbol{r}) \\ &= -SJ_{AB}(\boldsymbol{r})[\cos(\boldsymbol{R}\cdot\boldsymbol{Q}+\phi) \\ &\quad + \cos\psi_A\cos\psi_B + \sin\psi_A\sin\psi_B] \\ &\quad - \frac{S}{2}J_{AA}(\boldsymbol{r})[\sin(\boldsymbol{R}\cdot\boldsymbol{Q})\sin\psi_A\sin(\boldsymbol{k}\cdot\boldsymbol{r}) \\ &\quad + (\cos^2\psi_A\cos(\boldsymbol{R}\cdot\boldsymbol{Q}) + \sin^2\psi_A) \\ &\quad - \frac{1}{2}(\cos(\boldsymbol{R}\cdot\boldsymbol{Q})(1+\sin^2\psi_A) + \cos^2\psi_A)\cos(\boldsymbol{k}\cdot\boldsymbol{r})] \\ &\quad - \frac{S}{2}J_{BB}(\boldsymbol{r})[\sin(\boldsymbol{R}\cdot\boldsymbol{Q})\sin\psi_B\sin(\boldsymbol{k}\cdot\boldsymbol{r}) \\ &\quad + (\cos^2\psi_B\cos(\boldsymbol{R}\cdot\boldsymbol{Q}) + \sin^2\psi_B) \\ &\quad - \frac{1}{2}(\cos(\boldsymbol{R}\cdot\boldsymbol{Q})(1+\sin^2\psi_B) + \cos^2\psi_B)\cos(\boldsymbol{k}\cdot\boldsymbol{r})],\end{aligned} \tag{A3a}$$

$$\begin{aligned}\Xi^x(\boldsymbol{k},\boldsymbol{R},\boldsymbol{r}) = \frac{S}{2}&J_{AB}(\boldsymbol{r})[\{\cos(\boldsymbol{R}\cdot\boldsymbol{Q}+\phi)(1+\sin\psi_A\sin\psi_B) \\ &+ \cos\psi_A\cos\psi_B\}\cos(\boldsymbol{k}\cdot\boldsymbol{r}) \\ &- \sin(\boldsymbol{R}\cdot\boldsymbol{Q}+\phi)(\sin\psi_A+\sin\psi_B)\sin(\boldsymbol{k}\cdot\boldsymbol{r})],\end{aligned} \tag{A3b}$$

$$\begin{aligned}\Xi^y(\boldsymbol{k},\boldsymbol{R},\boldsymbol{r}) = -\frac{S}{2}&J_{AB}(\boldsymbol{r})[\{\cos(\boldsymbol{R}\cdot\boldsymbol{Q}+\phi)(1+\sin\psi_A\sin\psi_B) \\ &+ \cos\psi_A\cos\psi_B\}\sin(\boldsymbol{k}\cdot\boldsymbol{r}) \\ &+ \sin(\boldsymbol{R}\cdot\boldsymbol{Q}+\phi)(\sin\psi_A+\sin\psi_B)\cos(\boldsymbol{k}\cdot\boldsymbol{r})],\end{aligned} \tag{A3c}$$

$$\begin{aligned}\Xi^z(\boldsymbol{k},\boldsymbol{R},\boldsymbol{r}) = &-\frac{S}{2}J_{AA}(\boldsymbol{r})[\sin(\boldsymbol{R}\cdot\boldsymbol{Q})\sin\psi_A\sin(\boldsymbol{k}\cdot\boldsymbol{r}) \\ &+ (\cos^2\psi_A\cos(\boldsymbol{R}\cdot\boldsymbol{Q}) + \sin^2\psi_A) \\ &- \frac{1}{2}(\cos(\boldsymbol{R}\cdot\boldsymbol{Q})(1+\sin^2\psi_A) \\ &+ \cos^2\psi_A)\cos(\boldsymbol{k}\cdot\boldsymbol{r})] \\ &+ \frac{S}{2}J_{BB}(\boldsymbol{r})[\sin(\boldsymbol{R}\cdot\boldsymbol{Q})\sin\psi_B\sin(\boldsymbol{k}\cdot\boldsymbol{r}) \\ &+ (\cos^2\psi_B\cos(\boldsymbol{R}\cdot\boldsymbol{Q}) + \sin^2\psi_B) \\ &- \frac{1}{2}(\cos(\boldsymbol{R}\cdot\boldsymbol{Q})(1+\sin^2\psi_B) + \cos^2\psi_B) \\ &\times \cos(\boldsymbol{k}\cdot\boldsymbol{r})],\end{aligned} \tag{A3d}$$

where $\Xi^z(\boldsymbol{k},\boldsymbol{R},\boldsymbol{r}) = 0$ if $J_{AA} = J_{BB}$ and $\psi_A = \psi_B$. Similarly, the coefficients for $\Pi(\boldsymbol{k},\boldsymbol{R},\boldsymbol{r})$ are written as

$$\begin{aligned}\Pi^0(\boldsymbol{k},\boldsymbol{R},\boldsymbol{r}) = &\frac{S}{4}(\cos(\boldsymbol{R}\cdot\boldsymbol{Q})-1)\cos(\boldsymbol{k}\cdot\boldsymbol{r}) \\ &(J_{AA}(\boldsymbol{r})\cos^2\psi_A + J_{BB}(\boldsymbol{r})\cos^2\psi_B),\end{aligned} \tag{A3e}$$

$$\begin{aligned}\Pi^x(\boldsymbol{k},\boldsymbol{R},\boldsymbol{r}) = &\frac{S}{2}J_{AB}(\boldsymbol{r})[(\cos(\boldsymbol{R}\cdot\boldsymbol{Q}+\phi)(\sin\psi_A\sin\psi_B-1) \\ &+ \cos\psi_A\cos\psi_B)\cos(\boldsymbol{k}\cdot\boldsymbol{r}) \\ &- i\sin(\boldsymbol{R}\cdot\boldsymbol{Q}+\phi)(\sin\psi_A-\sin\psi_B) \\ &\times \cos(\boldsymbol{k}\cdot\boldsymbol{r})],\end{aligned} \tag{A3f}$$

$$\begin{aligned}\Pi^y(\boldsymbol{k},\boldsymbol{R},\boldsymbol{r}) = &-\frac{S}{2}J_{AB}(\boldsymbol{r})[(\cos(\boldsymbol{R}\cdot\boldsymbol{Q}+\phi)(\sin\psi_A\sin\psi_B-1) \\ &+ \cos\psi_A\cos\psi_B)\sin(\boldsymbol{k}\cdot\boldsymbol{r}) \\ &- i\sin(\boldsymbol{R}\cdot\boldsymbol{Q}+\phi)(\sin\psi_A \\ &- \sin\psi_B)\sin(\boldsymbol{k}\cdot\boldsymbol{r})],\end{aligned} \tag{A3g}$$

$$\begin{aligned}\Pi^z(\boldsymbol{k},\boldsymbol{R},\boldsymbol{r}) = &\frac{S}{4}(\cos(\boldsymbol{R}\cdot\boldsymbol{Q})-1)\cos(\boldsymbol{k}\cdot\boldsymbol{r}) \\ &\times (J_{AA}(\boldsymbol{r})\cos^2\psi_A - J_{BB}(\boldsymbol{r})\cos^2\psi_B).\end{aligned} \tag{A3h}$$

Here we find that $\mathrm{Im}\Pi^x(\boldsymbol{k},\boldsymbol{R},\boldsymbol{r})$ and $\mathrm{Im}\Pi^y(\boldsymbol{k},\boldsymbol{R},\boldsymbol{r})$ depend on $\sin\psi_A - \sin\psi_B$ and $\sin(\boldsymbol{R}\cdot\boldsymbol{Q}+\phi)$. Thus, these are nonzero only if $\psi_A \neq \psi_B$ and $\sin(\boldsymbol{R}\cdot\boldsymbol{Q}+\phi) \neq 0$. The expression for Π^z indicates that $\Pi^z(\boldsymbol{k},\boldsymbol{R},\boldsymbol{r})$ vanishes if $\psi_A = \psi_B$ and $J_{AA} = J_{BB}$ is satisfied.

Next, we write $H_0(\boldsymbol{k})$ as

$$H_0 = \begin{pmatrix} \Xi_0 & \Pi_0 \\ \Pi_0^* & \Xi_0^* \end{pmatrix}$$

and expand Ξ_0 and Π_0 as

$$\begin{aligned}\Xi_0 &= \Xi_0^0\sigma_0 + \Xi_0^x\sigma_x + \Xi_0^y\sigma_y + \Xi_0^z\sigma_z, \\ \Pi_0 &= \Pi_0^0\sigma_0 + \Pi_0^x\sigma_x + \Pi_0^y\sigma_y + \Pi_0^z\sigma_z,\end{aligned}$$

where each coefficient of the Pauli matrices is given as follows:

$$\begin{aligned}\Xi_0^0 = &\frac{S}{2}(\Delta_A(1-3\sin^2\psi_A) + \Delta_B(1-3\sin^2\psi_B)) \\ &+ \frac{h}{2}(\sin\psi_A + \sin\psi_B),\end{aligned} \tag{A4a}$$

$$\begin{aligned}\Xi_0^z = &\frac{S}{2}(\Delta_A(1-3\sin^2\psi_A) - \Delta_B(1-3\sin^2\psi_B)) \\ &+ \frac{h}{2}(\sin\psi_A - \sin\psi_B),\end{aligned} \tag{A4b}$$

$$\Pi_0^0 = \frac{S}{2}(\Delta_A\cos^2\psi_A + \Delta_B\cos^2\psi_B), \tag{A4c}$$

$$\Pi_0^z = \frac{S}{2}(\Delta_A\cos^2\psi_A - \Delta_B\cos^2\psi_B), \tag{A4d}$$

$$\Xi_0^x = \Xi_0^y = \Pi_0^x = \Pi_0^y = 0. \tag{A4e}$$

Here Ξ_0^z is zero if $\psi_A = \psi_B$. The above terms imply that if A and B sites are equivalent (i.e., $J_{AA} = J_{BB}$, $\Delta_A = \Delta_B$, and $\theta_A = \theta_B$), $\Xi^z(\boldsymbol{k},\boldsymbol{R},\boldsymbol{r}) = \Pi^z(\boldsymbol{k},\boldsymbol{R},\boldsymbol{r}) = \mathrm{Im}\Pi^i(\boldsymbol{k},\boldsymbol{R},\boldsymbol{r}) = \Xi_0^z = \Pi_0^z = 0$. Thus, the Hamiltonian satisfies the symmetry Eq. (14) leading to the vanishing Berry curvature.

Now, we consider the effective TRS $H(\boldsymbol{k}) = H^*(-\boldsymbol{k})$. In the above expressions, we can see that terms proportional to $\sin \boldsymbol{k}\cdot\boldsymbol{r}$ for the real part and $\cos \boldsymbol{k}\cdot\boldsymbol{r}$ for the imaginary part lead to the broken effective TRS. These terms are proportional to $\sin(\boldsymbol{R}\cdot\boldsymbol{Q})\sin\psi_i$ [see Eqs. (A3a) and (A3d)], $\sin(\boldsymbol{R}\cdot\boldsymbol{Q}+\phi)(\sin\psi_A + \sin\psi_B)$ [see Eqs. (A3b) and (A3c)], and $\sin(\boldsymbol{R}\cdot\boldsymbol{Q}+\phi)(\sin\psi_A - \sin\psi_B)$ [see Eqs. (A3f) and (A3g)]. Thus, $\boldsymbol{R}\cdot\boldsymbol{Q} = 0$ and $\boldsymbol{R}\cdot\boldsymbol{Q}+\phi = 0$ for all $\boldsymbol{R}$ or $\sin\psi_A = \sin\psi_B = 0$ support the effective TRS. This condition is independent from that for the effective PT symmetry and leads to the vanishing thermal Hall conductivity even if we have the nonzero Berry curvature. For instance, when $\boldsymbol{R}\cdot\boldsymbol{Q}+\phi = 0$ for all $\boldsymbol{R}$ or $\sin\psi_A = \sin\psi_B = 0$, we can still break the effective PT symmetry with $J_{AA} \neq J_{BB}$ (or $\Delta_A \neq \Delta_B$), via nonzero $\Xi^z(\boldsymbol{k},\boldsymbol{R},\boldsymbol{r})$ (nonzero Ξ_0^z).

The above expressions are applicable to the general BdG Hamiltonians of AB sublattice systems in the spiral phase. Once we consider the specific model, we assign a concrete value to $J_{\alpha\beta}$; For example, in J_1-J_2-J_2' model, J_{AB} with $|\boldsymbol{r}| = a$ is J_1 for the nearest-neighbor i, j sites, and J_{AA} (J_{BB}) with $|\boldsymbol{r}| = \sqrt{3}a$ is J_2 (J_2') for the next-nearest-neighbor sites.

Furthermore, we calculate the part of the magnon Hamiltonian for the DM interaction of the following form:

$$H_{\mathrm{DM}} = \sum_{i,j} D_{\alpha\beta}(\boldsymbol{S}_i \times \boldsymbol{S}_j)_z.$$

Here, we again consider the spiral phase and rewrite H_{DM} by $\boldsymbol{S}'$, which results in

$$H_{\mathrm{DM}} = \sum_{i,j} D_{\alpha\beta}\big[\cos\theta_{ij}\big(\sin\psi_i S_i'^x S_j'^y - \sin\psi_j S_j'^x S_i'^y\big) + \sin\theta_{ij}\big\{\sin\psi_i\sin\psi_j S_i'^x S_j'^x + S_i'^y S_j'^y + \cos\psi_i\cos\psi_j S_i'^z S_j'^z\big\}\big].$$

Using the HP transformation and the Fourier transformation, we obtain the DM interaction of magnons. The DM interaction term is also 4×4 BdG matrix of the form

$$H_{\mathrm{DM}}(\boldsymbol{k},\boldsymbol{R},\boldsymbol{r}) = \begin{pmatrix} \Xi_{\mathrm{DM}}(\boldsymbol{k},\boldsymbol{R},\boldsymbol{r}) & \Pi_{\mathrm{DM}}(\boldsymbol{k},\boldsymbol{R},\boldsymbol{r}) \\ \Pi_{\mathrm{DM}}^*(-\boldsymbol{k},\boldsymbol{R},\boldsymbol{r}) & \Xi_{\mathrm{DM}}^*(-\boldsymbol{k},\boldsymbol{R},\boldsymbol{r}) \end{pmatrix}.$$

Then, using Pauli matrices, we expand $\Xi_{\mathrm{DM}}(\boldsymbol{k},\boldsymbol{R},\boldsymbol{r})$ and $\Pi_{\mathrm{DM}}(\boldsymbol{k},\boldsymbol{R},\boldsymbol{r})$ as

$$\Xi_{\mathrm{DM}}(\boldsymbol{k},\boldsymbol{R},\boldsymbol{r}) = \Xi_{\mathrm{DM}}^0(\boldsymbol{k},\boldsymbol{R},\boldsymbol{r})\sigma_0 + \Xi_{\mathrm{DM}}^x(\boldsymbol{k},\boldsymbol{R},\boldsymbol{r})\sigma_x + \Xi_{\mathrm{DM}}^y(\boldsymbol{k},\boldsymbol{R},\boldsymbol{r})\sigma_y + \Xi_{\mathrm{DM}}^z(\boldsymbol{k},\boldsymbol{R},\boldsymbol{r})\sigma_z,$$

$$\Pi_{\mathrm{DM}}(\boldsymbol{k},\boldsymbol{R},\boldsymbol{r}) = \Pi_{\mathrm{DM}}^0(\boldsymbol{k},\boldsymbol{R},\boldsymbol{r})\sigma_0 + \Pi_{\mathrm{DM}}^x(\boldsymbol{k},\boldsymbol{R},\boldsymbol{r})\sigma_x + \Pi_{\mathrm{DM}}^y(\boldsymbol{k},\boldsymbol{R},\boldsymbol{r})\sigma_y + \Pi_{\mathrm{DM}}^z(\boldsymbol{k},\boldsymbol{R},\boldsymbol{r})\sigma_z,$$

where each coefficient of the Pauli matrices is as follows:

$$\begin{aligned}\Xi_{\mathrm{DM}}^0(\boldsymbol{k},\boldsymbol{R},\boldsymbol{r}) &= -SD_{AB}(\boldsymbol{r})\sin(\boldsymbol{R}\cdot\boldsymbol{Q}+\phi)\cos\psi_A\cos\psi_B \\ &\quad + \frac{S}{2}D_{AA}(\boldsymbol{r})[\cos(\boldsymbol{R}\cdot\boldsymbol{Q})\sin\psi_A\sin(\boldsymbol{k}\cdot\boldsymbol{r}) - \cos^2\psi_A \\ &\quad \times \sin(\boldsymbol{R}\cdot\boldsymbol{Q}) + \frac{1}{2}\sin(\boldsymbol{R}\cdot\boldsymbol{Q})(1+\sin^2\psi_A)\cos(\boldsymbol{k}\cdot\boldsymbol{r})] \\ &\quad + \frac{S}{2}D_{BB}(\boldsymbol{r})[\cos(\boldsymbol{R}\cdot\boldsymbol{Q})\sin\psi_B\sin(\boldsymbol{k}\cdot\boldsymbol{r}) - \cos^2\psi_B \\ &\quad \times \sin(\boldsymbol{R}\cdot\boldsymbol{Q}) + \frac{1}{2}\sin(\boldsymbol{R}\cdot\boldsymbol{Q})(1+\sin^2\psi_B)\cos(\boldsymbol{k}\cdot\boldsymbol{r})],\end{aligned} \tag{A5a}$$

$$\begin{aligned}\Xi_{\mathrm{DM}}^x(\boldsymbol{k},\boldsymbol{R},\boldsymbol{r}) &= \frac{S}{2}D_{AB}(\boldsymbol{r})[\sin(\boldsymbol{R}\cdot\boldsymbol{Q}+\phi)(1+\sin\psi_A\sin\psi_B)\cos(\boldsymbol{k}\cdot\boldsymbol{r}) \\ &\quad + \cos(\boldsymbol{R}\cdot\boldsymbol{Q}+\phi)(\sin\psi_A+\sin\psi_B)\sin(\boldsymbol{k}\cdot\boldsymbol{r})],\end{aligned} \tag{A5b}$$

$$\begin{aligned}\Xi_{\mathrm{DM}}^y(\boldsymbol{k},\boldsymbol{R},\boldsymbol{r}) &= \frac{S}{2}D_{AB}(\boldsymbol{r})[\sin(\boldsymbol{R}\cdot\boldsymbol{Q}+\phi)(1+\sin\psi_A\sin\psi_B)\sin(\boldsymbol{k}\cdot\boldsymbol{r}) \\ &\quad - \cos(\boldsymbol{R}\cdot\boldsymbol{Q}+\phi)(\sin\psi_A+\sin\psi_B)\cos(\boldsymbol{k}\cdot\boldsymbol{r})],\end{aligned} \tag{A5c}$$

$$\begin{aligned}\Xi_{\mathrm{DM}}^z(\boldsymbol{k},\boldsymbol{R},\boldsymbol{r}) &= \frac{S}{2}D_{AA}(\boldsymbol{r})[\cos(\boldsymbol{R}\cdot\boldsymbol{Q})\sin\psi_A\sin(\boldsymbol{k}\cdot\boldsymbol{r}) \\ &\quad - \cos^2\psi_A\sin(\boldsymbol{R}\cdot\boldsymbol{Q}) \\ &\quad + \frac{1}{2}\sin(\boldsymbol{R}\cdot\boldsymbol{Q})(1+\sin^2\psi_A)\cos(\boldsymbol{k}\cdot\boldsymbol{r})] \\ &\quad - \frac{S}{2}D_{BB}(\boldsymbol{r})[\cos(\boldsymbol{R}\cdot\boldsymbol{Q})\sin\psi_B\sin(\boldsymbol{k}\cdot\boldsymbol{r}) \\ &\quad - \cos^2\psi_B\sin(\boldsymbol{R}\cdot\boldsymbol{Q}) \\ &\quad + \frac{1}{2}\sin(\boldsymbol{R}\cdot\boldsymbol{Q})(1+\sin^2\psi_B)\cos(\boldsymbol{k}\cdot\boldsymbol{r})],\end{aligned} \tag{A5d}$$

$$\begin{aligned}\Pi_{\mathrm{DM}}^0(\boldsymbol{k},\boldsymbol{R},\boldsymbol{r}) &= -\frac{S}{4}\sin(\boldsymbol{R}\cdot\boldsymbol{Q})\cos(\boldsymbol{k}\cdot\boldsymbol{r}) \\ &\quad \times (D_{AA}(\boldsymbol{r})\cos^2\psi_A + D_{BB}(\boldsymbol{r})\cos^2\psi_B),\end{aligned} \tag{A5e}$$

$$\begin{aligned}\Pi_{\mathrm{DM}}^x(\boldsymbol{k},\boldsymbol{R},\boldsymbol{r}) &= \frac{S}{2}D_{AB}(\boldsymbol{r})[\sin(\boldsymbol{R}\cdot\boldsymbol{Q}+\phi)(\sin\psi_A\sin\psi_B - 1) \\ &\quad \times \cos(\boldsymbol{k}\cdot\boldsymbol{r}) + i\cos(\boldsymbol{R}\cdot\boldsymbol{Q}+\phi) \\ &\quad \times (\sin\psi_B - \sin\psi_A)\cos(\boldsymbol{k}\cdot\boldsymbol{r})],\end{aligned} \tag{A5f}$$

$$\begin{aligned}\Pi_{\mathrm{DM}}^y(\boldsymbol{k},\boldsymbol{R},\boldsymbol{r}) &= \frac{S}{2}D_{AB}(\boldsymbol{r})[\sin(\boldsymbol{R}\cdot\boldsymbol{Q}+\phi)(\sin\psi_A\sin\psi_B - 1) \\ &\quad \times \sin(\boldsymbol{k}\cdot\boldsymbol{r}) + i\cos(\boldsymbol{R}\cdot\boldsymbol{Q}+\phi) \\ &\quad \times (\sin\psi_B - \sin\psi_A)\sin(\boldsymbol{k}\cdot\boldsymbol{r})],\end{aligned} \tag{A5g}$$

$$\begin{aligned}\Pi_{\mathrm{DM}}^z(\boldsymbol{k},\boldsymbol{R},\boldsymbol{r}) &= -\frac{S}{4}\sin(\boldsymbol{R}\cdot\boldsymbol{Q})\cos(\boldsymbol{k}\cdot\boldsymbol{r}) \\ &\quad \times (D_{AA}(\boldsymbol{r})\cos^2\psi_A - D_{BB}(\boldsymbol{r})\cos^2\psi_B).\end{aligned} \tag{A5h}$$

Here $\Xi_{\mathrm{DM}}^z(\boldsymbol{k},\boldsymbol{R},\boldsymbol{r})$ and Π_{DM}^z are nonzero if $\psi_A \neq \psi_B$ or $D_{AA} \neq D_{BB}$, while $\mathrm{Im}\Pi_{\mathrm{DM}}^x(\boldsymbol{k},\boldsymbol{R},\boldsymbol{r})$ and $\mathrm{Im}\Pi_{\mathrm{DM}}^y(\boldsymbol{k},\boldsymbol{R},\boldsymbol{r})$ are nonzero only if $\psi_A \neq \psi_B$. We note that $\mathrm{Im}\Pi_{\mathrm{DM}}^x(\boldsymbol{k},\boldsymbol{R},\boldsymbol{r})$ and $\mathrm{Im}\Pi_{\mathrm{DM}}^y(\boldsymbol{k},\boldsymbol{R},\boldsymbol{r})$ are nonzero even if $\sin(\boldsymbol{R}\cdot\boldsymbol{Q}+\phi)$ is zero, in contrast to the Heisenberg term [$\mathrm{Im}\Pi^x(\boldsymbol{k}, \boldsymbol{R}, \boldsymbol{r})$ and $\mathrm{Im}\Pi^y(\boldsymbol{k}, \boldsymbol{R}, \boldsymbol{r})$].

From these terms, we can see that $D_{AA} \neq D_{BB}$ break the symmetry Eq. (14). Furthermore, $\Pi^z_{\mathrm{DM}}(\boldsymbol{k}, \boldsymbol{R}, \boldsymbol{r})$ contains the $\sin(\boldsymbol{k} \cdot \boldsymbol{r})$ terms, which can be nonzero even in the collinear phase where $\psi_A = \pm\psi_B = \pi/2$ and $\boldsymbol{Q} = 0$. In these cases, the DM interaction acts as the virtual magnetic field and generate nonzero Berry curvature (see Sec. II E).

[1] A. V. Chumak, V. Vasyuchka, A. Serga, and B. Hillebrands, Magnon spintronics, Nat. Phys. **11**, 453 (2015).
[2] T. Jungwirth, X. Marti, P. Wadley, and J. Wunderlich, Antiferromagnetic spintronics, Nat. Nanotechnol. **11**, 231 (2016).
[3] V. Baltz, A. Manchon, M. Tsoi, T. Moriyama, T. Ono, and Y. Tserkovnyak, Antiferromagnetic spintronics, Rev. Mod. Phys. **90**, 015005 (2018).
[4] J. Xiao, G. E. W. Bauer, K.-c. Uchida, E. Saitoh, and S. Maekawa, Theory of magnon-driven spin Seebeck effect, Phys. Rev. B **81**, 214418 (2010).
[5] V. A. Zyuzin and A. A. Kovalev, Magnon Spin Nernst Effect in Antiferromagnets, Phys. Rev. Lett. **117**, 217203 (2016).
[6] R. Cheng, S. Okamoto, and D. Xiao, Spin Nernst Effect of Magnons in Collinear Antiferromagnets, Phys. Rev. Lett. **117**, 217202 (2016).
[7] Y. Shiomi, R. Takashima, and E. Saitoh, Experimental evidence consistent with a magnon Nernst effect in the antiferromagnetic insulator $MnPS_3$, Phys. Rev. B **96**, 134425 (2017).
[8] H. Katsura, N. Nagaosa, and P. A. Lee, Theory of the Thermal Hall Effect in Quantum Magnets, Phys. Rev. Lett. **104**, 066403 (2010).
[9] Y. Onose, T. Ideue, H. Katsura, Y. Shiomi, N. Nagaosa, and Y. Tokura, Observation of the magnon Hall effect, Science **329**, 297 (2010).
[10] R. Matsumoto and S. Murakami, Rotational motion of magnons and the thermal Hall effect, Phys. Rev. B **84**, 184406 (2011).
[11] R. Matsumoto and S. Murakami, Theoretical Prediction of a Rotating Magnon Wave Packet in Ferromagnets, Phys. Rev. Lett. **106**, 197202 (2011).
[12] R. Matsumoto, R. Shindou, and S. Murakami, Thermal Hall effect of magnons in magnets with dipolar interaction, Phys. Rev. B **89**, 054420 (2014).
[13] Y. Zhang, S. Okamoto, and D. Xiao, Spin-Nernst effect in the paramagnetic regime of an antiferromagnetic insulator, Phys. Rev. B **98**, 035424 (2018).
[14] S. Park and B.-J. Yang, Topological magnetoelastic excitations in noncollinear antiferromagnets, Phys. Rev. B **99**, 174435 (2019).
[15] P. Laurell and G. A. Fiete, Magnon thermal Hall effect in kagome antiferromagnets with Dzyaloshinskii-Moriya interactions, Phys. Rev. B **98**, 094419 (2018).
[16] H. Doki, M. Akazawa, H.-Y. Lee, J. H. Han, K. Sugii, M. Shimozawa, N. Kawashima, M. Oda, H. Yoshida, and M. Yamashita, Spin Thermal Hall Conductivity of a Kagome Antiferromagnet, Phys. Rev. Lett. **121**, 097203 (2018).
[17] A. Mook, J. Henk, and I. Mertig, Thermal Hall effect in noncollinear coplanar insulating antiferromagnets, Phys. Rev. B **99**, 014427 (2019).
[18] S. A. Owerre, Topological thermal Hall effect in frustrated kagome antiferromagnets, Phys. Rev. B **95**, 014422 (2017).
[19] S. A. Owerre, Noncollinear antiferromagnetic Haldane magnon insulator, J. Appl. Phys. **121**, 223904 (2017).
[20] T. Ideue, Y. Onose, H. Katsura, Y. Shiomi, S. Ishiwata, N. Nagaosa, and Y. Tokura, Effect of lattice geometry on magnon Hall effect in ferromagnetic insulators, Phys. Rev. B **85**, 134411 (2012).
[21] M. Kawano and C. Hotta, Thermal Hall effect and topological edge states in a square-lattice antiferromagnet, Phys. Rev. B **99**, 054422 (2019).
[22] I. Dzyaloshinsky, A thermodynamic theory of "weak" ferromagnetism of antiferromagnetics, J. Phys. Chem. Solids **4**, 241 (1958).
[23] T. Moriya, Anisotropic superexchange interaction and weak ferromagnetism, Phys. Rev. **120**, 91 (1960).
[24] S. A. Owerre, Topological magnon bands and unconventional thermal Hall effect on the frustrated honeycomb and bilayer triangular lattice, J. Phys.: Condens. Matter **29**, 385801 (2017).
[25] F. A. Gómez Albarracín, H. D. Rosales, and P. Pujol, Chiral phase transition and thermal Hall effect in an anisotropic spin model on the kagome lattice, Phys. Rev. B **103**, 054405 (2021).
[26] S. A. Owerre, Magnon Hall effect without Dzyaloshinskii–Moriya interaction, J. Phys.: Condens. Matter **29**, 03LT01 (2017).
[27] K.-S. Kim, K. H. Lee, S. B. Chung, and J.-G. Park, Magnon topology and thermal Hall effect in trimerized triangular lattice antiferromagnet, Phys. Rev. B **100**, 064412 (2019).
[28] Y. Gao, X.-P. Yao, and G. Chen, Topological phase transition and nontrivial thermal Hall signatures in honeycomb lattice magnets, Phys. Rev. Research **2**, 043071 (2020).
[29] M. Naka, S. Hayami, H. Kusunose, Y. Yanagi, Y. Motome, and H. Seo, Spin current generation in organic antiferromagnets, Nat. Commun. **10**, 4305 (2019).
[30] M. Naka, S. Hayami, H. Kusunose, Y. Yanagi, Y. Motome, and H. Seo, Anomalous Hall effect in κ-type organic antiferromagnets, Phys. Rev. B **102**, 075112 (2020).
[31] M. Naka, Y. Motome, and H. Seo, Perovskite as a spin current generator, Phys. Rev. B **103**, 125114 (2021).
[32] C. Lacroix, P. Mendels, and F. Mila, eds., *Introduction to Frustrated Magnetism* (Springer, Berlin, 2011), Vol. 164.
[33] J. Železný, Y. Zhang, C. Felser, and B. Yan, Spin-Polarized Current in Noncollinear Antiferromagnets, Phys. Rev. Lett. **119**, 187204 (2017).
[34] M. Kimata, H. Chen, K. Kondou, S. Sugimoto, P. K. Muduli, M. Ikhlas, Y. Omori, T. Tomita, A. H. MacDonald, S. Nakatsuji, and Y. Otani, Magnetic and magnetic inverse spin Hall effects in a non-collinear antiferromagnet, Nature (London) **565**, 627 (2019).
[35] B. Li, S. Sandhoefner, and A. A. Kovalev, Intrinsic spin Nernst effect of magnons in a noncollinear antiferromagnet, Phys. Rev. Research **2**, 013079 (2020).
[36] S. Park, N. Nagaosa, and B.-J. Yang, Thermal Hall effect, spin Nernst effect, and spin density induced by a thermal gradient in collinear ferrimagnets from magnon–phonon interaction, Nano Lett. **20**, 2741 (2020).
[37] T. Holstein and H. Primakoff, Field dependence of the intrinsic domain magnetization of a ferromagnet, Phys. Rev. **58**, 1098 (1940).

[38] H. Kondo, Y. Akagi, and H. Katsura, Non-Hermiticity and topological invariants of magnon Bogoliubov–de Gennes systems, Prog. Theor. Exp. Phys. **2020**, 12A104 (2020).
[39] M. E. Zhitomirsky and T. Nikuni, Magnetization curve of a square-lattice Heisenberg antiferromagnet, Phys. Rev. B **57**, 5013 (1998).
[40] E. Rastelli, A. Tassi, and L. Reatto, Non-simple magnetic order for simple Hamiltonians, Physica B+C **97**, 1 (1979).
[41] J. Fouet, P. Sindzingre, and C. Lhuillier, An investigation of the quantum J_1-J_2-J_3 model on the honeycomb lattice, Eur. Phys. J. B **20**, 241 (2001).
[42] A. Mulder, R. Ganesh, L. Capriotti, and A. Paramekanti, Spiral order by disorder and lattice nematic order in a frustrated Heisenberg antiferromagnet on the honeycomb lattice, Phys. Rev. B **81**, 214419 (2010).
[43] R. F. Bishop, P. H. Li, D. J. Farnell, and C. E. Campbell, The frustrated Heisenberg antiferromagnet on the honeycomb lattice: J_1-J_2 model, J. Phys.: Condens. Matter **24**, 236002 (2012).
[44] R. F. Bishop, P. H. Y. Li, O. Götze, J. Richter, and C. E. Campbell, Frustrated Heisenberg antiferromagnet on the honeycomb lattice: Spin gap and low-energy parameters, Phys. Rev. B **92**, 224434 (2015).
[45] Y. Doi, Y. Hinatsu, and K. Ohoyama, Structural and magnetic properties of pseudo-two-dimensional triangular antiferromagnets $Ba_3MSb_2O_9$ (M=Mn, Co, and Ni), J. Phys.: Condens. Matter **16**, 8923 (2004).
[46] Y. Shirata, H. Tanaka, A. Matsuo, and K. Kindo, Experimental Realization of a Spin-1/2 Triangular-Lattice Heisenberg Antiferromagnet, Phys. Rev. Lett. **108**, 057205 (2012).
[47] H. D. Zhou, C. Xu, A. M. Hallas, H. J. Silverstein, C. R. Wiebe, I. Umegaki, J. Q. Yan, T. P. Murphy, J.-H. Park, Y. Qiu, J. R. D. Copley, J. S. Gardner, and Y. Takano, Successive Phase Transitions and Extended Spin-Excitation Continuum in the S=1/2 Triangular-Lattice Antiferromagnet $Ba_3CoSb_2O_9$, Phys. Rev. Lett. **109**, 267206 (2012).
[48] T. Susuki, N. Kurita, T. Tanaka, H. Nojiri, A. Matsuo, K. Kindo, and H. Tanaka, Magnetization Process and Collective Excitations in the S=1/2 Triangular-Lattice Heisenberg Antiferromagnet $Ba_3CoSb_2O_9$, Phys. Rev. Lett. **110**, 267201 (2013).
[49] G. Quirion, M. Lapointe-Major, M. Poirier, J. A. Quilliam, Z. L. Dun, and H. D. Zhou, Magnetic phase diagram of $Ba_3CoSb_2O_9$ as determined by ultrasound velocity measurements, Phys. Rev. B **92**, 014414 (2015).
[50] J. Ma, Y. Kamiya, T. Hong, H. B. Cao, G. Ehlers, W. Tian, C. D. Batista, Z. L. Dun, H. D. Zhou, and M. Matsuda, Static and Dynamical Properties of the Spin-1/2 Equilateral Triangular-Lattice Antiferromagnet $Ba_3CoSb_2O_3$, Phys. Rev. Lett. **116**, 087201 (2016).
[51] P. A. Maksimov, M. E. Zhitomirsky, and A. L. Chernyshev, Field-induced decays in XXZ triangular-lattice antiferromagnets, Phys. Rev. B **94**, 140407(R) (2016).
[52] X. Li, Z. Zhang, and H. Zhang, High throughput study on magnetic ground states with Hubbard U corrections in transition metal dihalide monolayers, Nanoscale Adv. **2**, 495 (2020).
[53] A. Moreo, E. Dagotto, T. Jolicoeur, and J. Riera, Incommensurate correlations in the t-J and frustrated spin-1/2 Heisenberg models, Phys. Rev. B **42**, 6283 (1990).
[54] A. Chubukov, First-order transition in frustrated quantum antiferromagnets, Phys. Rev. B **44**, 392 (1991).
[55] E. Rastelli and A. Tassi, Nonlinear effects in the spin-liquid phase, Phys. Rev. B **46**, 10793 (1992).
[56] J. Ferrer, Spin-liquid phase for the frustrated quantum Heisenberg antiferromagnet on a square lattice, Phys. Rev. B **47**, 8769 (1993).
[57] H. A. Ceccatto, C. J. Gazza, and A. E. Trumper, Nonclassical disordered phase in the strong quantum limit of frustrated antiferromagnets, Phys. Rev. B **47**, 12329 (1993).
[58] J. Reuther, P. Wölfle, R. Darradi, W. Brenig, M. Arlego, and J. Richter, Quantum phases of the planar antiferromagnetic J_1–J_2–J_3 Heisenberg model, Phys. Rev. B **83**, 064416 (2011).